McNair Scholars Program

Ignite Your Future with McNair

2021-2022 • Volume 27

Editors
Ashley Cervantes
LaWanda Holt-Fields
Abel Velasquez

The Journal of Research Reports
is published annually by the
Wichita State University
McNair Scholars Program
1845 Fairmount
Wichita, Kansas 67260-0199

Administration

President..... Dr. Richard Muma
Vice President of Strategic Engagement and Planning..... Kaye Monk Morgan
Associate Vice President for Special Programs ..... Deltha Q. Colvin

From the Director

It is with honor that I present Volume 27 of the Journal of Research Reports, "Ignite Your Future with McNair." The articles featured in this journal represent the work of Program participants from the 2021-2022 grant year. As one reads these articles, the breadth of research interests is as diverse as the students served by our Program. The McNair staff and I could not be more pleased with the efforts that went into producing this meaningful and scholarly body of work.

The Program can only achieve these accomplishments with the support of university faculty, staff, and administrators. Through the guidance of research mentors who have been able to inspire our Scholars to complete research projects despite any obstacles they may have encountered and reach such great heights. We applaud their dedication to making undergraduate research a reality and supporting the students from the McNair Scholar Program. It has been said, "it takes a village to raise a child," and you are our "village." Thank You.

As we close the final year in a five-year grant cycle, 2017 – 2022, we are excited to continue the tradition of promoting undergraduate research on the campus of Wichita State University since 1995.

Within this journal, you will find the work of eleven (11) undergraduate students whom we are showcasing for the work they have done and their commitment to thinking outside of the box and performing outside of the classroom. There are full manuscripts and summaries. These research activities serve to cultivate and develop research skills, provide experience navigating the research process and to create and develop relationships with faculty that could potentially assist students in applying, being admitted, and enrolling into graduate programs. The high impact activity of scholarly research is supported to assist our Scholars by leveling the playing field in their pursuit and completion of doctoral studies.

A special thank you is given to the staff for their dedication to the Program and the students that we serve. Mr. Abel Velasquez, research coordinator. Ms. Ashley Cervantes, assistant director and student confidant. Ms. Carrie Hartzler, administrative specialist and all-around Program support. Lastly, Ms. Deltha Q. Colvin, Associate Vice President for Special Programs who provides unending support for me and the staff as a whole.

Finally, I congratulate the students on a job well done; their efforts do not go unnoticed. They have taken this opportunity to share their brilliance with the academic community. These scholars are the future of America and I thank them for the opportunity to serve as their director.

Table of Contents

WSU Administration

Research Manuscripts

Research Summaries

Research Manuscripts

Oral Material Hazard Risk Assessment

Ashley Bland *and*
Heidi VanRavenhorst-Bell, PhD, CPT
Human Performance Studies, Wichita State University

Abstract

The Iowa Oral Performance Instrument (IOPI) was developed in 1988 and is a reliable, safe, and user-friendly medical device with FDA clearance. Healthcare professionals often use the IOPI when working with patients who present concerns of an orofacial myofunctional disorder (OMD) such as dysphagia and obstructive sleep apnea. IOPI is a tool intended to gather objective tongue strength and tongue endurance measures that assist with diagnosis and further guide and monitor a patient's treatment plan. It is also used by healthcare providers as a therapy tool to perform region-specific lingual exercises (i.e., anterior, posterior). The IOPI is portable and convenient, but when the bulb encounters saliva, it does not always remain in a fixed position, which may negatively alter the quality of the results. Due to this unintended movement of the bulb, an "anti-slip patch" has been developed that can be added to pre-existing medical devices (i.e., the IOPI bulb) to prevent slippage and deliver more reliable region-specific lingual measures. A more stable IOPI bulb may further assist with the delivery of a more concise diagnosis and targeted region-specific lingual treatment plan for each patient. The objective of this study was to administer FDA-regulated usability and hazard risk assessments of an adhesive material "anti-slip patch" intended for use in the oral cavity in combination with known oral medical devices.

Introduction

The Iowa Oral Performance Instrument (IOPI) is a common device used to measure tongue strength and endurance (Adams, et al., 2013a; IOPI, 2021; VanRavenhorst-Bell et al., 2017, 2018), and offers the ability to assess the anterior and posterior regions of the oral tongue separately (Adams, et al., 2013b; IOPI, 2020; VanRavenhorst-Bell et al., 2017, 2018). The IOPI does this by providing a "numeric display of the pressure generated by pressing the tongue against an air-filled bulb" (Adams, et al., 2013a; Solomon et al., 2020). Originally created to measure the strength of the tongue in children (Luschei et al., *IOPI Medical* 2022), it is now commonly used in patients with dysphagia, often caused by neurogenic disorders such as stroke or Parkinson's disease, brain injury, and multiple sclerosis (Park et al., 2015). Some doctors prefer to measure patient tongue function subjectively. However, when creating rehabilitation programs, they are left looking for novel solutions. Subjective methods used in the past make it virtually impossible for health practitioners to maintain consistency. The IOPI, however, can be used as a consistent diagnostic device that also functions well for rehabilitation. Therefore, it is becoming more popular among medical providers. While the use of this device has helped many people since its creation in 1988, it has had one common complaint. When the soft rubber bulb encounters saliva within the oral cavity, it tends to shift and slip from its intended placement (Adams et al., 2013a; Solomon et al., 2020; VanRavenhorst-Bell et al., 2021). This concern about bulb slippage has further called the reliability of the IOPI device measurements into question (Adams et al. 2013a).

Efforts to address the bulb slippage led to the development of the anti-slip patch. This patch is a device that can be applied directly to an existing medical device, such as the IOPI bulb. The patch has a latex-free textured fabric surface that is adhered to the surface on one side of the bulb to prevent the device from slipping. Some reports have shown that slippage may cause inconsistent results, especially during tongue lateralization and tongue protrusion. Applying an anti-slip surface has been found to improve these tongue-strength assessments (Adams, et al., 2013a; Solomon et al., 2020;). In one study, participant perception of the anti-slip patch was recorded, and it found that persons perceived that the anti-slip patch reduced the overall slippage of the bulb during lingual functional testing (VanRavenhorst-Bell et al., 2021).

The patch is easy to manufacture and easy to apply by simply peeling the cover off the adhesive, applying the patch to the surface, and testing as normal (shown in Figures 1 and 2). It is a technology that has tremendous potential in the industry. However, despite promising results regarding the patch's effectiveness, FDA-regulated usability and hazard risk assessments must be administered before the patch can be widely used and accepted. This study tested adherence to FDA guidelines. For a device to be considered safe the FDA states,

> "There is reasonable assurance that a device is safe when it can be determined, based upon valid scientific evidence, that the probable benefits to health from the use of the device for its intended uses…

outweigh any probable risks. Among the types of evidence that may be required, when appropriate, to determine that there is reasonable assurance that a device is safe are investigations using laboratory animals, investigations involving human subjects, and nonclinical investigations including in vitro studies" (Center for Devices and Radiological Health, *FDA Medical devices*, n.d.).

To adhere to this definition, the study design simulated a patient-like environment. The study aimed to examine microbiological content, adhesive residue, and microbiological growth.

Figure 1. Images of IOPI Bulb without and with Anti-slip Patch attached

Figure 2. Insertion of the IOPI bulb into the Oral Cavity (IOPI Medical, 2021)

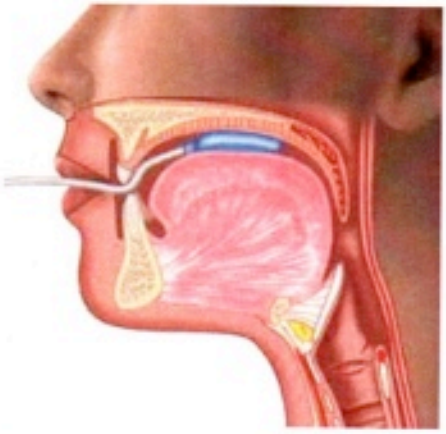

Methods

A 25 mL tube of saliva was first gathered and tested negatively for COVID-19 for safety assurance. Twenty-seven (n=27) IOPI bulbs were prepped across three conditions. Condition one (n=9) presented the IOPI bulb in its natural state and was labeled "No Patch-Wash", Condition two (n=9) presented the IOPI bulb with an anti-slip patch and was labeled "Patch-Wash", and Condition three (n=9) presented the IOPI bulb with an anti-slip patch and was labeled "Patch-No Wash." Each bulb was individually dipped into the 25 mL tube of saliva, then placed into their own tube rest for a predetermined amount of time: 15 minutes, 30 minutes, or 1 hour. Three trials per condition were completed across three different time periods. Each trial was administered concurrently, to keep conditions similar between trials.

As a bulb's allotted time expired, the bulb was removed from its tube. The bulbs labeled No Patch-Wash, and Patch-Wash were then cleaned with warm water and dawn dish soap for 30 seconds (per IOPI cleaning instructions provided with bulbs), then patted dry with a paper towel. The bulbs labeled Patch-No Wash were not cleaned and served as a control for comparison.

After the cleaning process was completed, each bulb was rolled onto a new and labeled sheep's blood agar plate. These plates were placed into a CO2 incubator at 37 degrees Celsius for 48 hours, then removed. Bacterial colonies were counted, recorded, and photographed, then the plates were placed in a refrigerator to keep them in their current growth state. This process is referred to as Batch 1 in the results section.

The IOPI bulbs were then placed back in their

labeled packaging and placed in a box for one week. On day seven the bulbs were removed from their storage location and rolled onto new sheep blood agar plates to investigate any changes in growth state from the prior week. This process is referred to as Batch 2 in the results section.

Analysis

To examine the difference in bacterial growth between each type of bulb, three separate repeated measures - Analysis of Variance (ANOVA) were conducted for Batch 1, Batch 2, and a comparison of Batch 1 to Batch 2. The significance level for each analysis was set to 0.05.

Results

A repeated measures-ANOVA analysis of Batch 1 colony count with Sphericity assumed found a significant difference in bacterial count between *Conditions* main effect, $F(2,4)= 7,247.73$, $p= 0.001$*, $n_p^2= 1.0$, power= 1.0, while the main effect of *Time*, $F(2,4)= 0.891$, $p= 0.479$, $n_p^2= 0.31$, power= 0.12 and interaction (time x condition) $F(4,8)= 0.385$, $p= 0.814$, $n_p^2= 0.16$, power= 0.10 were not found to be significant (*see* Figure 5). Post hoc comparisons of the main effect *Condition* further showed that the Patch-No Wash had a significantly higher count of bacteria compared to Patch-Wash and No Patch-Wash ($p= 0.001$, $p= 0.001$), respectively as shown in Table 1. No significant difference was found between Patch-Wash and No Patch-Wash ($p= 1.000$).

Figure 3: Microbiological count comparison following a 15-minute, 30-minute, and 1-hour saliva bat

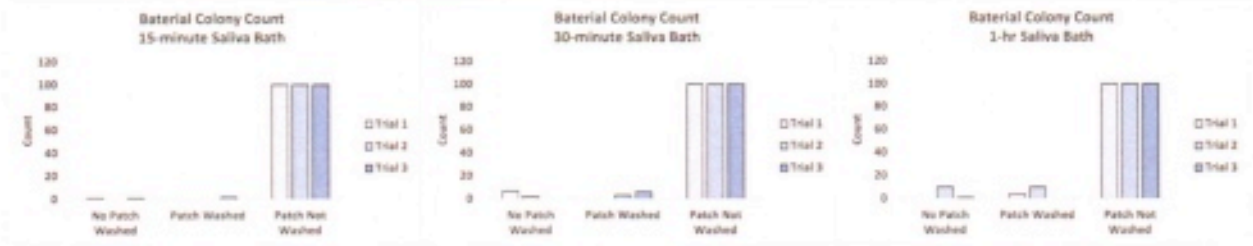

Table 1: Batch 1 colony count post saliva bath for each condition across time			
15 Minutes			
Trial	**Patch/No Wash**	**Patch/Wash**	**No Patch/Wash**
T1	>100	0	1
T2	>100	0	0
T3	>100	2	1
30 minutes			
Trial	**Patch/No Wash**	**Patch/Wash**	**No Patch/Wash**
T1	>100	0	7
T2	>100	3	2
T3	>100	6	0
1 Hour			
Trial	**Patch/No Wash**	**Patch/Wash**	**No Patch/Wash**
T1	>100	4	0
T2	>100	10	10
T3	>100	0	1

A repeated measures-ANOVA analysis of Batch 2 colony count with Sphericity not assumed and a Greenhouse-Geisser administered found similar findings as Batch 1 analysis with a significant difference in bacterial count between *Conditions* main effect, $F(1,2)= 59667.63$, $p< 0.001$*, $n_p^2= 1.0$, power= 1.00, while the main effect of *Time*, $F(1,2)= 1.000$, $p= 0.423$, $n_p^2= 0.333$, power= 0.095, and interaction (time x condition) $F(1,2)= 1.000$, $p= 0.423$, $n_p^2= 0.333$, power= 1.00 were not found to be significant. Post hoc comparisons of the main effect *Condition* further showed that the Patch-No Wash had a significantly higher count of bacteria compared to Patch-Wash and No Patch-Wash ($p= 0.001$, $p= 0.001$), respectively as shown in Table 2. No significant difference was found between Patch-Wash and No Patch-Wash ($p= 1.000$).

Table 2. Batch 2 colony count post saliva bath for each condition across time

15 minutes			
Trial	**Patch/No wash**	**Patch/Wash**	**No Patch/Wash**
T1	100	0	0
T2	100	0	0
T3	100	0	1
30 minutes			
Trial	**Patch/No wash**	**Patch/Wash**	**No Patch/Wash**
T1	100	0	0
T2	100	0	0
T3	100	1	0
1 hour			
Trial	**Patch/No wash**	**Patch/Wash**	**No Patch/Wash**
T1	100	0	0
T2	100	0	0
T3	100	0	3

A third repeated measures-ANOVA was administered to evaluate changes in the colony from Batch 1 to Batch 2. As shown in Figure 4, the *Condition* main effect, $F(8,32)= 3121.155$, $p< 0.001$*, $n_p^2= 0.999$, power= 1.00, and the between main effect *Batch* were found to be significant, $F(1,4)= 7.875$, $p= 0.049$, $n_p^2= 0.663$, power= 0.565. Post hoc comparison showed Batch 1 (m=35.074 $\pm$ 0.392) presented with a significantly higher count of bacterial colonies than Batch 2 (m=33.519 $\pm$ 0.392) (*see* Figure 5). The interaction (condition x batch) $F(8,32)= 0.955$, $p= 0.487$, $n_p^2= 0.193$, power= 0.363 was not significant. Post hoc comparisons of the main effect *Condition* showed Patch-No Wash had a significantly higher count of bacteria compared to Patch-Wash and No Patch-Wash ($p= 0.001$, $p= 0.001$), respectively. No significant difference was found between Patch-Wash and No Patch-Wash ($p= 1.000$).

Figure 4. Microbiological count comparison following a 15-minute, 30-minute, and 1-hour saliva bath between Batch 1 and Batch 2.

Figure 5. Microbiological Growth of Batch 1 and Batch 2 across Time and Condition by Trial.

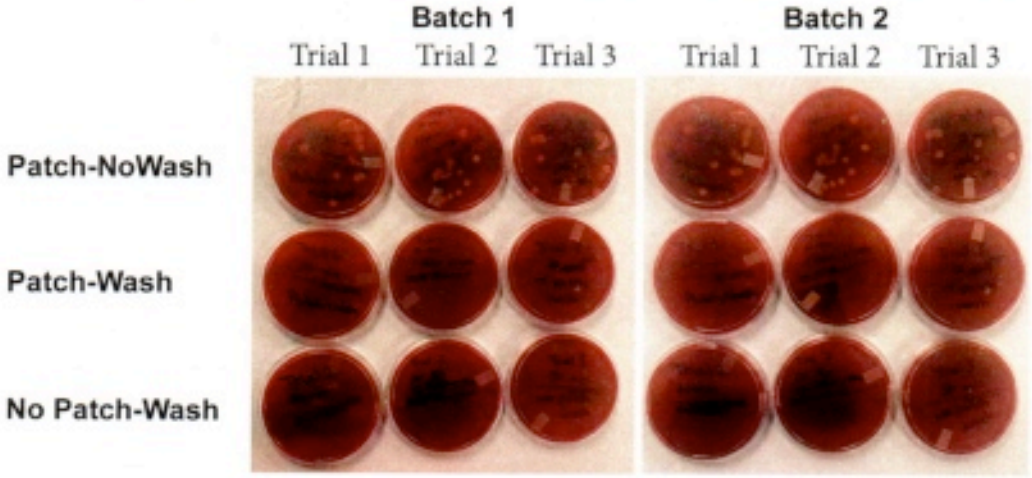

Discussion

For a device to be considered safe according to the FDA, there must be reasonable assurance, based upon scientific evidence, that the probable benefits to health from the use of the device outweigh any probable risks (Center for Devices and Radiological Health, *FDA Medical devices*, n.d.).

Therefore, this study is the first phase in an ongoing study, with the priority to determine if the anti-slip patch adds unwanted risks to the existing IOPI bulb biohazard risk procedures in place. For example, the current study monitored microbiological activity on the IOPI bulb after being exposed to saliva and then washed or not washed to ensure that microbe levels did not increase with the addition of the anti-slip patch.

Overall, the findings showed that adding an anti-slip patch to an IOPI bulb did not significantly increase microbiological risk with saliva exposure. More specifically, the findings were favorable for use of the anti-slip patch with the IOPI bulb, displaying comparable microbial values as the IOPI bulb with no patch. After exposure to saliva and then being properly washed, each bulb (No Patch-Washed, Patch-Washed) grew normal amounts of oral flora, as shown in Figure 6. Interestingly, the variability of the raw colony count across trials 1-3 within a condition and time period was of concern. One possible explanation may be due to potential inconsistencies in the washing

process. Although a set washing protocol (e.g., clean with warm water and dawn dish soap for 30-seconds) was implemented, some bulbs may have been more thoroughly cleaned than others.

In addition, the findings showed significantly lower microbial colonies count on the IOPI bulb washed and the IOPI bulb with a patch washed compared to the bulb with a patch that was not washed; further suggesting that the anti-slip patch does not present as a biohazardous risk. Rather the absence of washing the bulb (patch or no patch) increases the risk of excessive microbial colonies. The test (Batch 1)–retest (Batch 2) findings further indicated that when a bulb is properly washed, the application of the anti-slip patch on the bulb did not significantly increase the risk of microbial growth even after the anti-slip patch remained on the IOPI bulb for an additional 7-days (*see* Figure 5).

The test-retest of bulb conditions across time was important because it simulated an unfavorable practice that a clinician/doctor may allow. For example, a bulb is commonly issued to "a patient" and reused across multiple visits. Following the first office visit, the bulb with or without the anti-slip patch may or may not be washed and then placed in a drawer to sit until the patient was to return for his/her next appointment. This practice may invite an elevated presence of microbial colonies on the bulb when the anti-slip patch is attached; therein, heightening one's risk of illness.

Unexpectedly, after removing the bulbs from the simulated dark and isolated environment, the follow-up (Batch 2, 7-day post) plating grew significantly less flora (p=0.049) than during the first plating (Batch 1). This was surprising, considering most bacteria thrive in warm, moist, dark environments. One hypothesis of this unexpected finding was that the anti-slip patch may have contained antibiotics. To test this theory, a copy of the anti-slip patch was made, and a lawn of streptococcus aureus was grown with the patch placed in the middle of the blood agar plate. As expected, a zone of inhibition developed around the anti-slip patch on the plate. This confirmed that the anti-slip patch contained some form of antibiotic. For a medical device designed to be implemented orally, it should not contain antibiotics unintentionally. Due to this finding, this study will be repeated with a non-antibiotic anti-slip patch intended for use orally.

Conclusion

Overall, the objective of this study was to test the generic FDA medical device definition, which involved determining if the anti-slip patch added any unnecessary risks or negative effects when used on the IOPI bulb. When solely evaluating microbiological content as well as adhesive residue, there was virtually no difference between these groups. The anti-slip patch did not aid in the growth of bacteria on the surface of the IOPI bulb, nor did it add abrasive residue upon removal. Due to these results, it appears that the anti-slip patch may function well as a solution to the IOPI bulb's tendency to slip, contributing only positive effects.

This version of the anti-slip patch, however, did contain antibiotics and is most likely not the best option for common use within the oral cavity in patients with an Orofacial Myofunctional Disorder. Further studies are required to evaluate the anti-slip patch without antibiotics.

References

Adams, V., Mathisen, B., Baines, S., Lazarus, C., & Callister, R. (2013a). A systematic review and meta-analysis of measurements of tongue and hand strength and endurance using the Iowa Oral Performance Instrument (IOPI). *Dysphagia*, *28*(3), 350–369. https://doi.org/10.1007/s00455-013-9451-3

Adams, V., Mathisen, B., Baines, S., Lazarus, C., & Callister, R. (2013b). Reliability of measurements of tongue and hand strength and endurance using the Iowa oral performance instrument with Healthy Adults. *Dysphagia*, *29*(1), 83–95. https://doi.org/10.1007/s00455-013-9486-5

Center for Devices and Radiological Health. (n.d.). *FDA Medical devices*. U.S. Food and Drug Aministration. Retrieved May 31, 2022, from https://www.fda.gov/medical-devices

Explore IOPI Pro. IOPI Medical. (2020, June 15). Retrieved April 5, 2022, from https://iopimedical.com/explore-pro/

IOPI Medical professionals. IOPI Medical. (2021, July 6). Retrieved June 9, 2022, from https://iopimedical.com/medical-professionals/

Luschei, E., & Mythen, T. (2022, May 31). IOPI Medical. Retrieved May 31, 2022, from https://iopimedical.com/

Park, J.-S., Kim, H.-J., & Oh, D.-H. (2015). Effect of tongue strength training using the Iowa oral performance instrument in stroke patients with dysphagia. *Journal of Physical Therapy Science*, *27*(12), 3631–3634. https://doi.org/10.1589/jpts.27.3631

Solomon, N., & Clark, H. (2020). The effect of an anti-slip surface on objective measures of tongue strength in healthy adults. *International Journal of Orofacial Myology and Myofunctional Therapy*, *46*(1), 13–21. https://doi.org/10.52010/ijom.2020.46.1.2

VanRavenhorst-Bell, H. A., Coufal, K. L., Patterson, J. A., & Mefferd, A. S. (2018). A comparative study: Tongue muscle performance in weightlifters and runners. *Physiological Reports*, *6*(22). https://doi.org/10.14814/phy2.13923

VanRavenhorst-Bell, H. A., Mefferd, A. S., Coufal, K. L., Scudder, R., & Patterson, J. (2017). Tongue strength and endurance: Comparison in active and non-active young and older adults. *International Journal of Speech-Language Pathology*, *19*(1), 77–86. https://doi.org/10.3109/17549507.2016.1154983

VanRavenhorst-Bell, H., & Cook, L. (2021). Perceptions of tongue-bulb comfort and stability with and without anti-slip patches during assessments of tongue strength and endurance. *International Journal of Orofacial Myology*, *47*(1), 14–21. https://doi.org/10.52010/ijom.2021.47.1.3

Beam-line Study for CueSat NIAC Phase III

Octavio Pacheco-Vazquez *and*
Nick Solomey, PhD

Department of Mathematics & Statistics, Wichita State University

Abstract

Neutrino detector development for space flight has been under NIAC phase III sponsorship since August of 2021. The purpose of this phase is to build a test detector, i.e. CubeSat, which will be placed into Earth's Orbit at some point in 2024. The purpose of the CubeSat is to test the shielding, electronics, and GAGG crystal in space. A bigger detector will be built in the future to be launched near the sun and detect neutrinos. This paper focuses on the study of the beam-line particle accelerator, where protons and electrons have been shot at the device from various angles through simulations. With the help of a platform (Geant4) that simulates particles going through a given volume and ROOT, used for data analysis, both a visual and mathematical method has been developed. The mathematical method implemented is called Bhattacharyya Distance Method. These tools help study the effects and relationships of the particles going through the CubeSat, as well as help us identify what type of particle interacted with the detector, what direction it came from, and its energy. Results show that it is possible to find relationships with an error of less than 0.5%.

Introduction

Neutrinos have been a subatomic particle of interest to scientists since they were predicted nearly 100 years ago. Scientists have created models that explain natural phenomena by studying neutrino interactions. Many other discoveries have been possible thanks to the studying of neutrinos including imaging the inside of the Sun. However, the work is not fully complete. In the last 20 years, it was discovered that neutrinos hold a very small amount of mass, as opposed to being massless as it was previously presumed. In the last 10 years, scientists discovered three flavors, or three different kinds, of neutrinos. Several laboratories around the world are currently studying solar neutrinos. However, scientists have yet to propose a correct model for the ongoing fission processes in our Sun. Understanding how our nearest star works will help us understand other distant stars in space.

Some neutrino detectors have been built specifically to observe solar neutrinos. This subatomic particle travels through space at almost the speed of light. It only takes them about eight minutes to travel from the Sun to the Earth, much faster than other particles that may take up to thousands of years to reach the Earth. This makes neutrinos a good resource to study the Sun, however, they seldom interact with the detectors here on Earth, making research difficult. The primary goal of this research is to inform the construction of two devices that will be launched near the Sun to observe solar neutrinos much closer to the source.

The method to detect neutrinos chosen for this research is called the Double Pulse method. This project uses the Gallium-Germanium interaction for the detector. When an electron neutrino interacts with a particular Gallium isotope with sufficient energy, the reaction causes a neutron to become a proton, and it also produces an electron. As a proton is produced, the Gallium (Ga) becomes the next heavier element, Germanium (Ge). Considering only the interactions with a certain minimum energy threshold, Ge will be left in an excited state with a couple of different mean lifetimes, depending on the Ge isotope; Ge will then go back to its ground state liberating a gamma particle with it. The first pulse comes from the production of the electron, the second pulse comes from the Ge in the excited state going back to its ground state.

Sending these types of detectors near the Sun requires significant research. This project is focused on building a smaller detector, about the size of a loaf of bread, that will be launched into a polar orbit around the Earth. The size of this new detector will be significantly smaller than the other detectors that currently exist on Earth. Launching a neutrino detector to space can be compared to the Hubble Telescope. The Hubble telescope is much smaller when compared to other telescopes in observatories on Earth, but, as it is not being blocked by Earth's atmosphere, it becomes the most powerful existing telescope.

This smaller detector is called a CubeSat. The CubeSat is NASA's initiative that allows small satellites to fly on scheduled rocket launches. The launch is scheduled for 2024. This detector will be a smaller version of the detectors that will be launched near the Sun. The main purpose of this smaller device is to check the functionality of the detector's equipment outside the magnetic shielding of the Earth. Because of the size of the

CubeSat, it is not expected to detect any neutrinos, but by applying a "fake" double pulse method, it will be possible to observe similar interactions with other particles and cosmic rays.

Literature Review

Nearly one hundred years ago, scientists encountered a puzzling problem involving beta decay as it appeared to break the Law of Conservation of Energy. The law states that the energy of a system, such as potential and kinetic energy, must not change before or after an interaction. The alpha decay was well defined and had a nice peak of energy distribution, whereas the beta decay had a broad energy distribution with some missing energy. Some scientists questioned the Law of Conservation and suspected that the conservation of energy was something statistical. Swedish professor Wolfgang Pauli speculated about the existence of yet another type of subatomic particle that would account for this "missing" energy yet not be detected. Pauli wasn't very proud of this speculation as suggesting the existence of something that cannot be detected contradicted his work and reputation as a theoretical physicist. However, he was right, there was a missing particle. This new particle was called **neutrino** (Solomey 1997). The purpose of this paper is to outline what is known about neutrinos and inform a future research project to add to the body of knowledge about this particle.

Neutrinos are an exciting and mysterious type of subatomic particle. As it turns out, neutrinos are one of the most common particles in our universe. The existence of neutrinos was predicted nearly 100 years ago, but they were not proven conceptually until 30 years later with the Cowen-Reines experiment in 1956. It took another 30 years to detect neutrinos in experiments (Larson 2006). Since then, researchers have worked to understand these particles. Even though neutrinos are very abundant, we still don't fully understand them. They are very small (nearly massless) and have no charge, and therefore, hardly ever interact with anything. They only interact via a weak nuclear force.

It is theorized that neutrinos were created less than a second after the creation of the universe; also, neutrinos are still being created in cataclysmic events such as supernovas and in the interior of some stars. As such, our Sun is a focus of research (Larson 2006). At the core of the stars, the temperatures and pressures are so great that fusion processes occur. The atoms of hydrogen found in the core of stars fuse together to form a heavier element, helium. During this process, neutrinos are created. We know there has been a neutrino interaction when a neutron converts itself into a proton and emits an electron and a neutrino. Enrico Fermi, with the collaboration of Wolfgang Pauli, named this interaction the "four-point" theory. You begin with one particle, and you get three different particles as a result (Solomey 1997).

Experiments, such as Helios I and II, have increased our understanding of solar processes at the core and at the other various layers of the Sun (Siddiqi, 2018). However, there are still some unknowns. Neutrinos rarely interact with matter. Therefore, neutrinos produced at the core of the Sun escape unchanged, making them a powerful tool to study the solar processes (Solomey 2017). Among other things, our project will also

enable us to create a 3D map of the inner layer of the Sun using the neutrino flux. In Figure 2 we see an image created by Neutrinos coming from the Sun using the Japanese detector Super Kamiokande. Neutrino detection is the preferred method because it only takes these particles about eight minutes to travel from the core of the Sun to the Earth, whereas other particles can take up to 10⁴ years to get to us from the center of the Sun (Larson 2006). Detecting neutrinos from the center of our nearest star will increase our understanding of other stars in the universe.

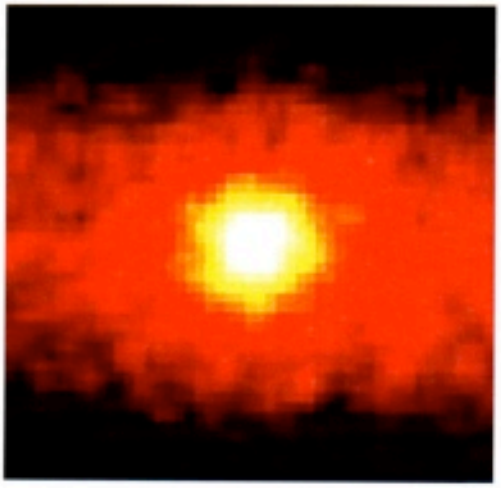

Figure 2: Image of the sun produced using the Super Kamiokande detector's neutrino data

For this reason, several neutrino detectors have been built or are being constructed currently around the globe. Those detectors include the Antarctic Impulsive Transient Antenna (ANITA), IceCube, Super-Kamiokande, Deep Underground Neutrino Experiment (DUNE), and Askaryan Radio Array (ARA). Most of the detectors built so far are large and heavy. IceCube, located at the South Pole, is about one cubic kilometer in size and was drilled about 2500 meters underground (IceCube Neutrino Observatory); Super-Kamiokande requires 50,000 tons of purified water surrounded by phototubes to detect Cherenkov Radiation (Larson 2006); DUNE has two underground facilities 1300-kilometer apparat that shoot particles from one to the other, one at Fermilab in Illinois and the other in Sanford Underground Research Facility in South Dakota with detectors adding up to 70,000 tons.

Neutrinos rarely interact with anything, making tremendously large detectors necessary in order to detect them from Earth. Some detectors are underground because that way you isolate your detectors from cosmic ray radiation and other types of background noise here on Earth. Substantial resources are needed to build the detector facilities to house them. Our project will be innovative because the detector will be smaller, and we will launch into space. By launching our detector into space, we get at least two advantages: 1) noise reduction from other particles and signals here on Earth and 2) reduction of the size and mass required for neutrino detectors here on Earth.

This research will help support building at least two detectors that will eventually go near the Sun to about three and seven solar radii, where the solar neutrino flux increases as shown in Figure 3. The closest stage to the research project is the construction of the CubeSat. The CubeSat is a device of about 30 x 10 x 10 cm that is planned to be launched into Earth's orbit in 2024. The CubeSat will start at a height of about 450 kilometers above the Earth (Solomey 2021). The dimensions of this detector are significantly smaller than other detectors. Launching a neutrino detector into space can be compared

to the Hubble Telescope (or to the James Webb telescope). The Hubble telescope is considerably smaller than observatories on Earth, but since it is not blocked by Earth's atmosphere, it is the most powerful telescope in existence.

Distance from Sun	Flux relative to Earth
696342 km ($R_\odot$)	46400
1500000 km ($\sim 3R_\odot$)	10000
4700000 km ($\sim 7R_\odot$)	1000
15000000 km	100
47434000 km	10
Mercury	6.7
Venus	1.9
Earth	1
Mars	0.4
Asteroid Belt	0.1
Jupiter	0.037
Saturn	0.011
Uranus	0.0027
Neptune	0.00111
Pluto	0.00064
KSP	0.0002
Voyager 1 (2015)	0.00006

Figure 3: Intensity of solar neutrinos at various distances from the Sun

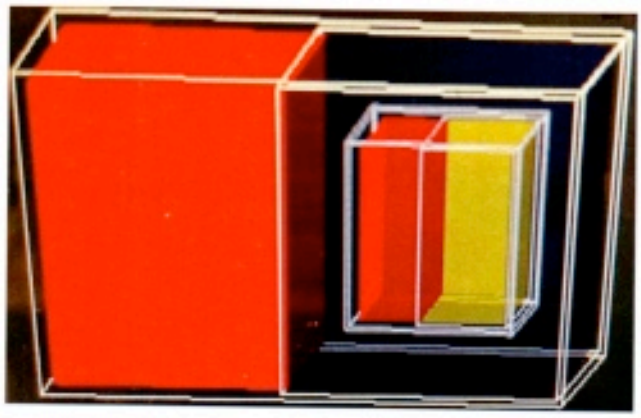

Figure 4: Sketch of CubeSat in the simulations

4. The large red rectangle represents the PMT, the smaller red piece is a silicon PMT, and the yellow rectangle represents the GAGG crystal. Those structures will be housed within a tungsten shield.

There are a few different methods of detecting neutrinos: Scintillators, Radiochemical methods, and Cherenkov detectors. Cherenkov detectors are devices in which particles are made to go through them at a higher speed than the speed of light in that medium, but still slower than the speed of light in a vacuum. Cherenkov detectors require large volumes of a clear material, such as water or ice, surrounded by light-sensitive photomultiplier tubes. A sufficiently charged lepton going through the detector creates a visible "optical shockwave" that the photomultiplier tubes detect and then the energy, direction, and sometimes the flavor of the neutrino are measured. The radiochemical method is a process in which beta decay is used. The preferred beta reactions are the Chlorine-Argon and Gallium-Germanium interactions. Our project will use the Gallium-Germanium interaction for our detector.

This research will use simulations from Geant4 to model the desired particle interactions using a Monte Carlo method (Solomey 2021). Large data sets will be analyzed to establish if there has been a neutrino interaction. This research will include real-life testing, in addition to the simulations with the Geant4, which will provide even more significant data. With this data, the team will be able to make changes to the detector components and sizes accordingly.

Methods

The primary goal of this research is to inform the design of two devices that will be launched near the Sun to detect neutrinos, to three and seven solar radii respectively. Getting that close to the nearest star to Earth will increase the neutrino flux by about a factor of 10000 and 1000 respectively. To detect solar neutrinos on Earth, scientists have built detectors that are miles long and weigh thousands of tons. The detectors on this project will be no larger than 7-8 feet and weigh much less than one ton. Such an ambitious project requires a lot of data taking and time. First, an even smaller detector will be built to test that the components and electronics work properly; this smaller detector is the CubeSat, scheduled to launch into a polar orbit around the Earth in 2024.

The CubeSat's main components are the detector itself, electronics, GPS, and power system. The team at Wichita State University is focused on the detector construction which will be a third of the length of the CubeSat (10 x 10 x 10 cm). The people from NASA, JPL, Nano Avionics, and other Universities are working on the rest of the device. The detector will consist of a mix of tungsten powder and epoxy working as the main shield of the detector, inside the detector will be a photomultiplier tube (PMT), a veto array, a coat of reflective material, a silicon PMT, and the Gadolinium Aluminum Gallium Garnet Crystal (GAGG) doped with Cerium, where the GAGG crystal is the actual detector.

GAGG crystals are fairly new material. They were first developed by the Japanese and put out on the market around 2014. After these crystals are exposed to 70 MeV, for a period between six months to 10 years, the crystal starts to glow. This is about the same energy level that a satellite in Low Earth Orbit (LEO) in an equatorial and Sun-synchronous orbit is exposed to. This luminescence causes some noise to the detections. The afterglow effect is caused by defects within the crystal's lattice.

The CubeSat has not been constructed yet. Most of the work has been simulation-based. One of the first tests before launching the satellite into orbit will be to take the CubeSat to the Fermilab National Laboratory and place it into the beamline. This will allow the researchers to rotate the CubeSat in any position and direct particles toward it from different angles, similar to how it would in space. This research has focused on simulating the particles obtained in the GAGG crystal when particles are shot at the CubeSat in the beamline.

Simulations

The simulations were run using Geant4 (from GEometry ANd Tracking) which is a C++ extension library, widely used for medicine and particle physics. Geant4 is very useful, as it shows realistic particle interactions which use a Monte-Carlo method through different functionalities of C++. ROOT Data Analysis Framework was used to analyze the data that was obtained from the simulations in Geant4. ROOT is a very powerful tool that is capable of using Python and R to create and manipulate histograms from large amounts of data. ROOT also provides accurate means and standard deviations that are helpful in obtaining more realistic results.

The code was programmed so every time a simulation was run on Geant4, a ROOT file was

created, which contained several histograms of our interest, such as: energy deposited in the veto array, energy deposited in the liquid scintillator, time the first photoelectron is detected, number of photoelectrons that reached a particular PMT, and other data. One special interest for this study was to look at the number of photoelectrons that reached each PMT and its standard deviation within and after the first 50ns to make sure the primary signal matched the desired time window, so neutrinos were analyzed properly.

At Fermilab, it will be easy to rotate the detector to the desired position giving a known angle from where the particle came from. This study did not use Fermilab's facilities, but that is the next step. When the CubeSat is in space, particles will enter the device from all directions. To figure out the angle and energy level at which the particle entered the detector, both a visual and a mathematical method have been implemented. The visual method consists of superimposing two histograms on top of each other based on the closeness of their mean standard deviation. Just by looking at the graphs, it is easy to assess similarities. The mathematical method implemented is called Bhattacharyya Distance Method, where the distance between two histograms is calculated first by using the following formula,

$$BC(p,q) = \sum_{x \in X} \sqrt{p(x)q(x)}$$

where BC(p, q) is the total sum of the product of the probabilities, p(x) is the probability of a bin from the first histogram to occur, and q(x) is the probability of a bin from the second histogram to occur. After figuring out BC(p, q) then the following formula is applied,

$$D_B(p,q) = -ln(BC(p,q))$$

where D_s(p,q) is the distance between the two plots. These formulas should return how close to each other the histograms are.

Data Collection

Several histograms have been obtained. Energy levels that ranged from 800MeV to 4000MeV were applied to the electrons and protons shot at the CubeSat. At each energy level, the detector was given five different angle rotations: 0.0, 22.5, 45.0, 67.5, and 90.0 degrees. These simulations were run using Beoshock, Wichita State's supercomputer. Unfortunately, the ROOT histograms obtained through Beoshock cannot be easily manipulated. Therefore, a C language file must be created to take the data in and to do the desired manipulations/operations.

To simulate a particle in space entering the detector from a random angle, a random number generator was coded to give the particle gun a random angle and location. The new histogram is obtained and then analyzed using visual and mathematical methods.

Analysis of Data

The first step, for both the electron and proton case, was to visually compare the histogram with the random angle to the histograms with the defined angles. For some plots, it is clear to see they hold no relationship. The second step was to look at the means obtained directly from ROOT. This allowed us to narrow down the potential range of angles which the random angle could have been generated from.

The next step was to create more plots between

the ranges of the means, with angles of increments of 4.5°. These new plots will be compared using the BC method. For instance, in a case where both plots were the same, from the BC(p,q) equation, the result would be equal to 1. Therefore, from the D, equation, the result would be 0, meaning that there is no distance between the plots, they are the same exact plot.

Results

Plots were created to simulate interactions of electrons and protons at varying energy levels at defined angles.

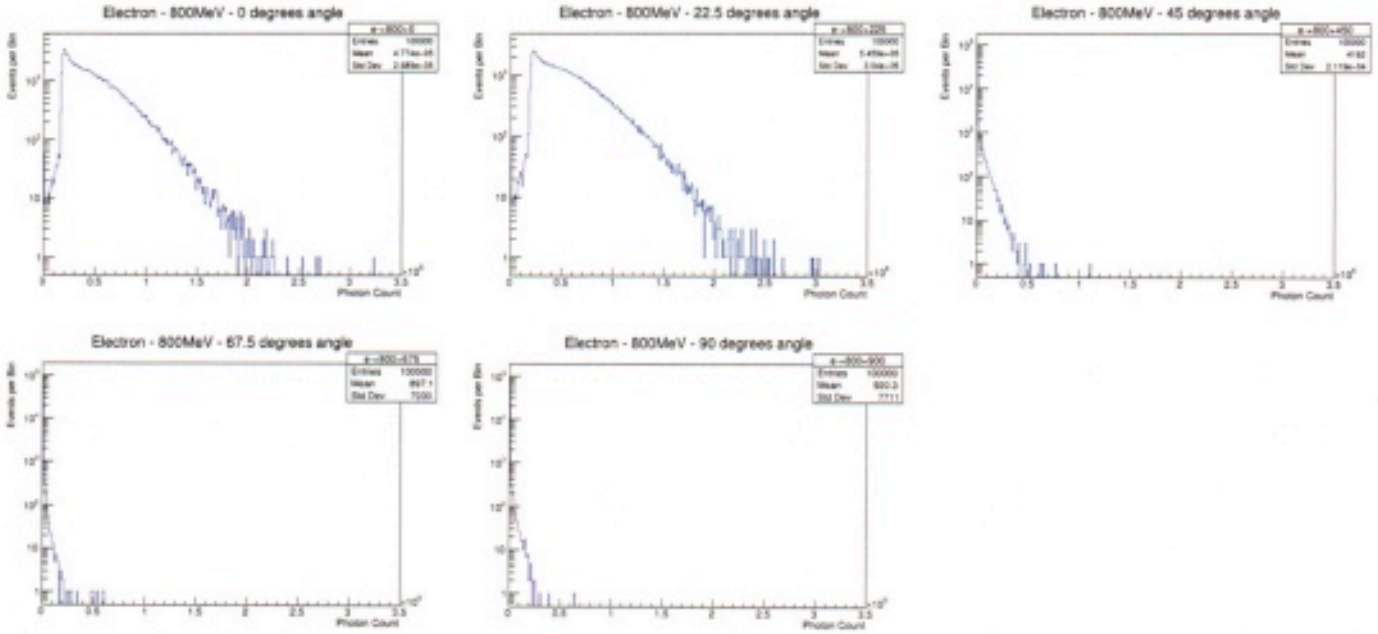

Figure 5: Low energy regime for electron

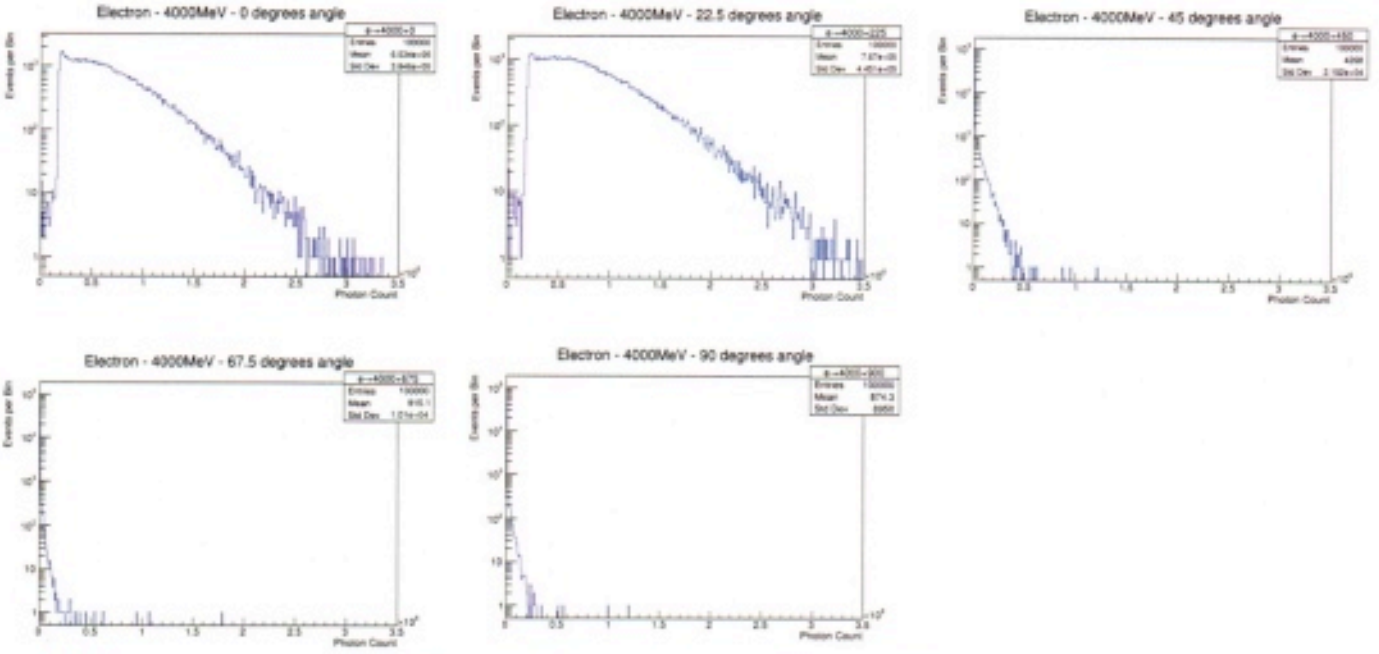

Figure 6: High energy regime for electron

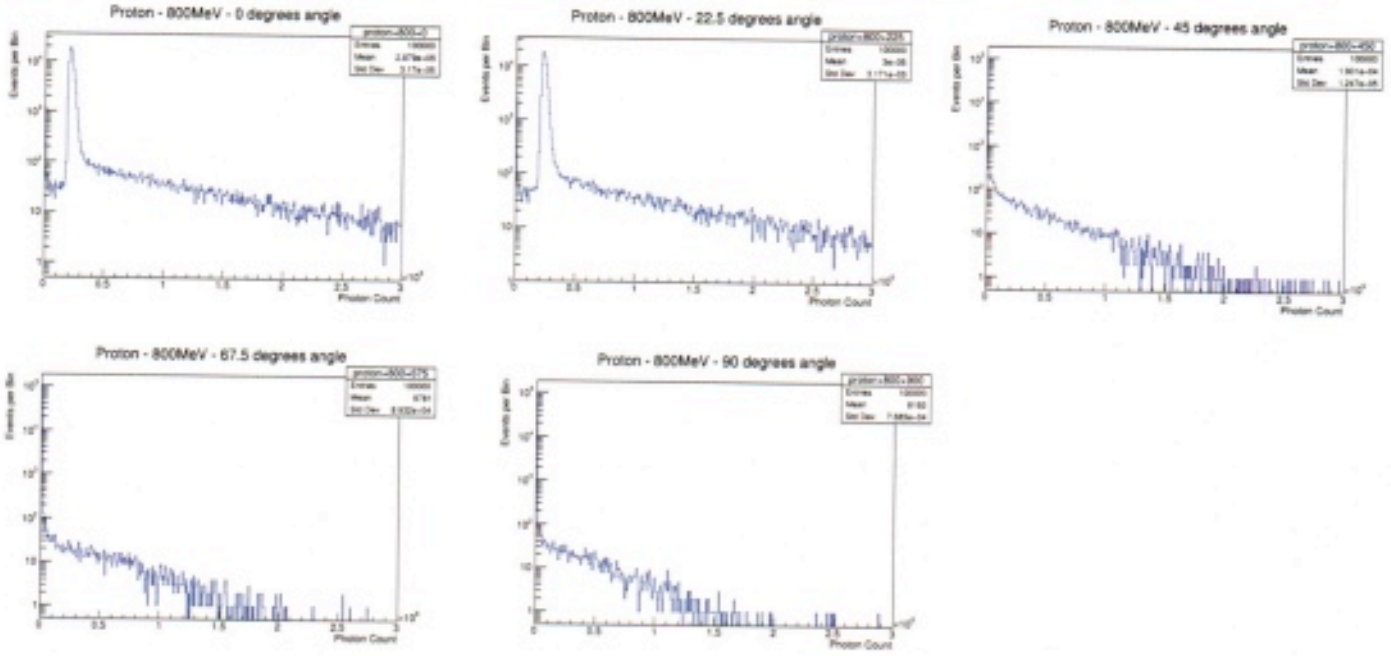

Figure 7: Low energy regime for proton

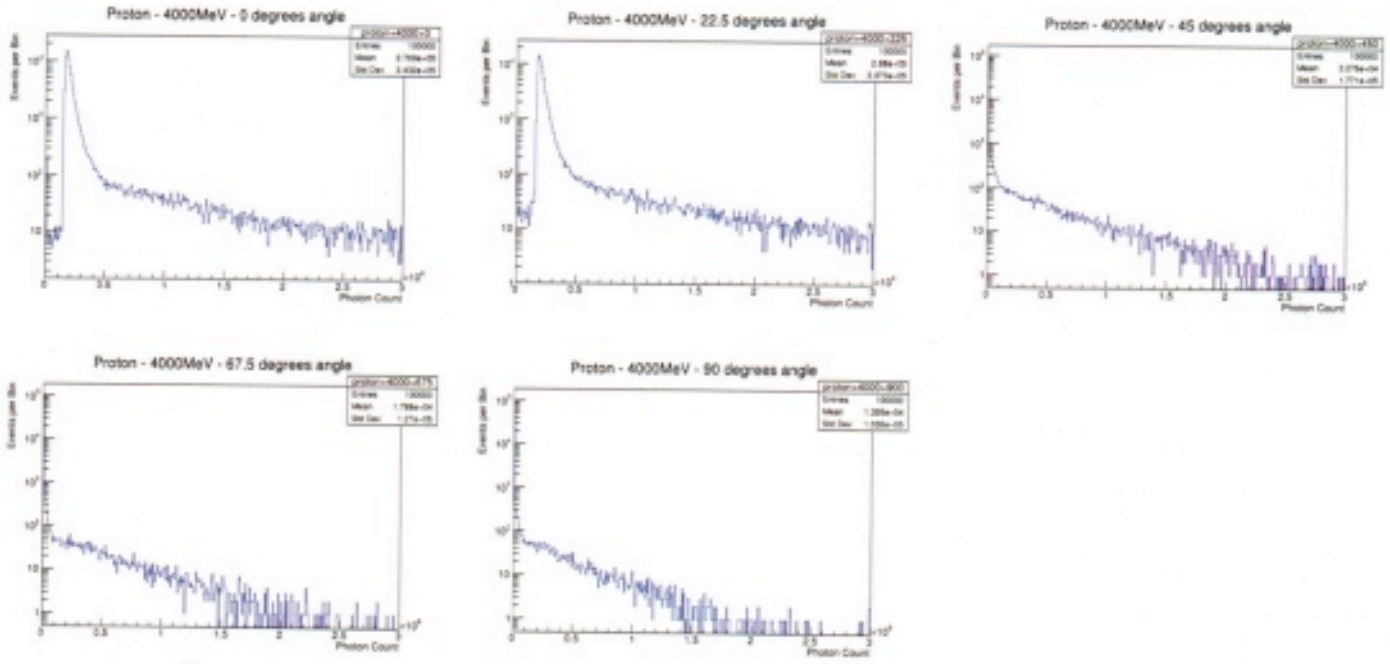

Figure 8: High energy regime for proton

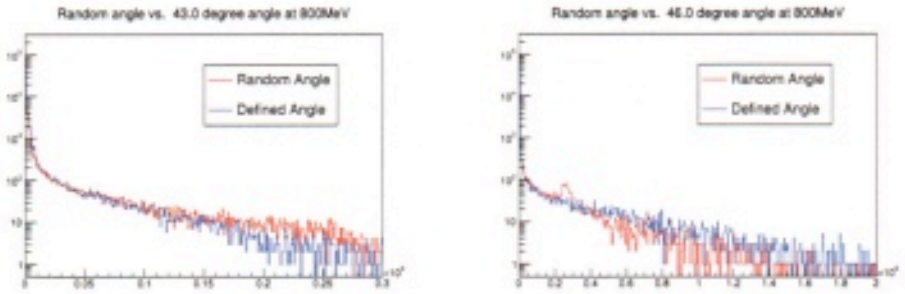

Figure 9: Visual comparison of proton

Energy	Angle	$BC(p,q)$	D_B
800MeV	45.0°	0.997625	0.00247783
	46.0°	0.99776	0.00224272
	47.0°	0.997712	0.00229059
	48.0°	0.997637	0.00236593
	49.0°	0.997687	0.00231518
900MeV	45.0°	0.997663	0.00233981
	46.0°	0.997809	0.00219367
	47.0°	0.997698	0.0023045
	48.0°	0.997732	0.002271
	49.0°	0.997649	0.00235332
1500MeV	45.0°	0.997451	0.00255184
	46.0°	0.997456	0.00254681
	47.0°	0.997449	0.00255436
	48.0°	0.997373	0.00263059
	49.0°	0.996919	0.00308594

Table 1: BC method for electron

Energy	Angle	$BC(p,q)$	D_B
800MeV	41.0°	0.993737	0.00628251
	42.0°	0.998589	0.00141152
	43.0°	0.998776	0.0012244
	44.0°	0.998157	0.00184423
	45.0°	0.997208	0.00279564
900MeV	41.0°	0.994047	0.00597115
	42.0°	0.998431	0.00157055
	43.0°	0.998943	0.00105804
	44.0°	0.998446	0.00155563
	45.0°	0.997512	0.00249062
1500MeV	41.0°	0.995519	0.00449065
	42.0°	0.9985	0.00150115
	43.0°	0.998906	0.00109455
	44.0°	0.998584	0.00141714
	45.0°	0.997746	0.0022564

Table 2: BC method for proton

Plots with a random angle at 800, 900, and 1500MeV were created using a random number generator in Geant4. These plots were compared to the plots with defined angles.

Discussion

Geant4 is a very powerful tool that can be used to simulate countless processes within the realm of high-energy physics. This project was able to simulate the interactions of electrons and protons going through the detector portion of the CubeSat, but the interactions inside the GAGG crystal were the focus of this study. Each run shot 100,000 electrons, or protons, to the detector. Histograms obtained with ROOT revealed the number of events vs. the optical photons created in the crystal.

In the electron case, the mean of the plot with the random angle suggested that the unknown angle was between the plots of 22.5° and 45.0°, but closer to the second angle. Then the BC method was applied for the shorter increments of the defined angles in between the two original ones. The results indicate that the unknown angle was between 41.0° and 45.0°. Finally, running increments of 1.0°,

the 43.0° produced the shortest BC distance with a percent error between the two plots of about 0.12%. In the proton case, the observation of the mean suggested that the random angle was between the 45.0° and 67.5° angle. Following a similar process as in the electron case, the angle was found at 46.0° with a corresponding 0.22% error. In both cases, the percent error is so small that one can be certain of the direction at which the particle entered the detector to the nearest degree, as well as the particle's energy level.

Limitations

This project has been computational so far. Geant4 is an excellent simulation program, but it may differ slightly from the results in the actual beamline. Since the beamline is manmade there is a margin of error that needs to be accounted for with what energy levels were used in the testing. This means that the CubeSat test results can be slightly skewed if the most accurate energy levels found in space are not used. Another potential limitation is that the code for the Cube-Sat is based on a Monte Carlo method, therefore even if the same exact event were to be run twice, the resulting plot would be slightly different.

Another limitation of this project was run-time and memory usage for the simulations. In some cases, it would take up to 24 hours to complete with a 192GB memory usage to get one single plot; this is a lot of time considering that more than 50 plots were obtained. Part of the problem with the time and memory was due to a memory leak inside the code used to run the simulations. There was an extra portion in the code that was not relevant to this portion of the project that slowed down the process. Unfortunately, this flaw was not discovered until near the end of the project. Most national laboratories or bigger universities have thousands of GB of memory at their disposal. Having access to more memory would allow us to run higher energy levels.

In the science and technology fields, there is always room for improvement and change; this project is no exception. The design used for this project has already been modified and improvements will continue. However, there was not enough time to have results from those modifications included here.

Future Research

The study of the beamline will be one of the major tests to know whether the CubeSat is ready to go to space. Future research should assess whether the predictions obtained with the simulations are correct according to the model and components of the satellite or if adjustments are needed. The most important components of the CubeSat are yet to be tested. Understanding the effects of having very energetic particles going through the detector will not only help build the bigger neutrino detector this research project aims toward in the future, but other projects will also be able to use this technology for their research.

The simulations were completed with the detector laying down on its side and rotating only about the vertical axis. Future work for this project includes taking into consideration a second axis rotation. Including a second axis, the rotation will allow the particles to enter the detector from a diagonal position, as opposed to just coming in from the same plane. It is planned that now for every angle rotation about

one axis, the same five original angle rotations will be given to the second axis. These will give the same number of plots as before times five.

New modifications of the design will be tested. Instead of having only one silicon PMT, four PMTs that increase the size of the original will replace it. Also, a Quartz window will be added in between the PMTs and the GAGG crystal. These updates are expected to provide better detections to particles that otherwise would not interact at all with the detector.

References

CERN, https://lbnf-dune.fnal.gov/about/overview/.

IceCube, https://icecube.wisc.edu/science/icecube/.

J. Folkerts, "Neutrino Detector Design, Attenuation Studies, and Testing for the vSol Project," Master's thesis, Wichita State University, 2020.

Larson, Neutrinos!, 2006, http://www.astro.wisc.edu/~larson/Webpage/neutrinos.html

N. Solomey, "Design and technical study of neutrino detector spacecraft," 2017.

N. Solomey, Nickolas. "Chapters 1 & 2." The Elusive Neutrino: A Subatomic Detective Story, Scientific American Library, New York, 1997.

N. Solomey, Folkerts, J., Meyer, H., Gimar, C., Novak, J., Doty, B., ... & Christl, M. (2022). Design of a Space-based Near-Solar Neutrino Detector for the $\nu $ SOL Experiment. arXiv preprint arXiv:2206.00703.

Siddiqi, Asif A. Beyond Earth: A Chronicle of Deep Space Exploration, 1958-2016. NASA History Program Office, 2018.

Research Summaries

Sexual Assault and Domestic Violence Prevention Education: Delivery in COVID-19

Estella Armenta *and*
Rachael Goodman-Williams, PhD
Psychology Department, Wichita State University

Introduction

Teen dating violence (TDV) is a public health issue that often occurs alongside other victimization experiences. According to a nationally representative Youth Risk Behavior Survey, of the students who reported dating over the last 12 months, 10% experienced physical dating violence and 11% experienced sexual dating violence (Kann, 2016). Forms of TDV are abuse from a caregiver, physical abuse, sexual assault, and witnessing victimization (Cheung & Huang, 2022). TDV increases the likelihood of risky behaviors like substance abuse and thoughts of suicide. In previous research, victimization of TDV is primarily experienced by girls (87.6%), while boys experience less (12.4%) (Dosil et al., 2020). All genders, ethnicities, and sexual orientations have reported instances of TDV. In the context of this study, prevention is used to diminish the chances of sexual assault and domestic violence (SA/DV) occurring.

Prevention education is the use of discussions and activities to prevent risky activities from happening. Prevention programming includes teaching students about the differences between healthy and unhealthy relationships, consent, inappropriate behavior, and how to report incidents (CDC, 2017). TDV can occur in a public setting or even at a family member's residence. Prevention educators are individuals from community agencies who deliver prevention education.

Once the COVID-19 pandemic started, primary prevention in the education system was disrupted. Prevention educators had to find different ways to reach their audiences. This study aims to find out "How did COVID-19 affect the delivery of SA/DV prevention education in middle and high schools in the Midwest?"

Methods

To recruit study participants, the Community Response to Sexual Assault (CRSA) lab team emailed the study details to sexual assault and domestic violence (SA/DV) state coalitions in a dozen Midwest states (IA, IL, IN, KS, MI, MN, MO, ND, NE, OH, SD, and WI). In the email, the research team asked the coalitions to relay the study details and information to the respective SA/DV community organizations. The research team relied on confirmation emails to secure participants. If they did not get a response, they sent out a second email. After the second round of emails, eleven of the twelve states agreed to share awareness of the study with community organizations. The research team spoke to and recruited participants from nine of the 12 states. Twenty prevention educators from the Midwest participated in semi-structured interviews. These prevention educators are employed at sexual assault (SA), domestic violence (DV), or dual SA/DV community agencies. Out of 20 participants, 17 worked at dual community agencies and three were employed at a DV-only community agency.

Participants were from Indiana (n=4), Kansas (n=2), Michigan (n=2), Minnesota (n=2), Missouri (n=1), Nebraska (n=1), Ohio (n=2), South Dakota (n=1), and Wisconsin (n=5). Prevention educators identified as white (85%), African American/Black (10%), and Latino/Hispanic (5%). Participants received $30 for participating in the study. The Institutional Review Board (IRB) from Wichita State University approved all research materials.

The average interview time was 60 minutes (M=57:53 minutes, SD=14:59 minutes). These were semi-structured interviews that included six sections: opening questions, curriculum selection, implementation and adaption of programs, reflections on prevention programming, questions regarding COVID-19, and demographic questions. Interviews were conducted over Zoom; audio recordings were made and imported to REV.com, a transcript cleaning program. CRSA lab team created several codes to organize the transcripts. During the content analysis, two main themes emerged: benefits and concerns.

Results

Twenty-eight benefits and 30 concern codes were identified through content analysis. In this study, "benefits" would be described as an aspect of change that a prevention educator found to be helpful while delivering prevention education. "Concerns" would be described as an aspect or change that a prevention educator found to be difficult while delivering prevention education. Three participants did not report any benefits, indicating that they had difficulty recognizing the potential benefits of their SA/DV prevention delivery methods.

While 28 benefits were reported, only six were reported more than once. Ten percent of participants found that making their programs visually engaging, using polls, using whiteboards including whiteboard apps, using pre-recorded videos, and using a Mentimeter presentation program benefited online instruction.

As for concerns, 30 were identified. There was more consistency found within concerns. Fourteen concerns were reported by prevention educators: prevention educators had to change everything, difficulty getting students engaged

in the material, they experienced a limited time to teach, they had fewer schools to teach, made kids wear headphones for the safety of themselves and others, past programs had a poor impact, prevention educators found teaching on the individual device to be difficult, online had poor performance, did not know if students were receiving material, had difficulty connecting amongst the group, online burnout, no requests from schools or counselors, students bullied other students, and not being able to read body language. These concerns reflect the difficulty of online teaching and learning in the pandemic environment. Half of the participants were concerned about lack of student engagement, 35% reported that online teaching is difficult. Twenty percent reported that they had to change their entire teaching style. Lastly, 25% reported that they had a limited time capacity to teach the material.

Conclusion

Prevention educators found some aspects of online delivery methods beneficial during COVID-19, such as private communication, accomplishing other projects, and working alongside other community agencies. Prevention educators were able to receive private messages from students through Zoom. These students were able to ask questions anonymously. Prevention educators were able to check in with specific students about uncomfortable situations they may have been experiencing. Delivering prevention education online provided students with more privacy and a place to talk about issues that they might not talk about in person. Prevention educators had to create other platforms to reach the students. The lack of access through schools gave prevention educators a chance to expand their prevention education onto other platforms like YouTube, podcasts, and TikTok. Students need to see this content to familiarize themselves with the concepts. The stigmatization of talking about these issues can be lessened over time. Students who receive this information can gain confidence about the subject and will be able to identify toxic behaviors that can lead to sexual assault and domestic violence. During COVID-19, prevention educators had opportunities to connect with other community agencies regarding SA/DV prevention education. The pandemic provided the opportunity for prevention educators and community agencies to brainstorm strategies to teach SA/DV prevention education effectively in a new format.

While there were benefits to being forced to use alternative delivery methods, there were also concerns and consequences that were reported. Some schools canceled prevention education altogether, while others shifted to online or remained in person with a shortened curriculum. Prevention educators had to remove certain topics due to time length and school preferences. Consequently, there is a varied level of knowledge within these Midwest states. Students did not all receive the same information. This is a concern because students who do not receive prevention education may not be able to identify risk factors within relationships, consent implications, and what to do in case of emergencies. These students are more susceptible to TDV (Eleby, 2009). Another concern regarding delivery is online burnout. Students attended their regular classes online and prevention programming

added another activity to their day. Prevention educators also faced Zoom fatigue. According to Williams (2021), reports show that professionals have a reduced ability to read body language, detect humor, and other social cues through Zoom. Overall, professionals face occupational distress because of new technology (Williams, 2021). This affects student engagement. Another concern about teaching this curriculum online was that other individuals could hear the materials. A sibling might listen, without context, or more importantly, parents who could be abusive might hear them. To avoid burnout, a more exploratory online video program might make content more interesting. Interactive prevention education strategies could engage students in more different, relevant, and exciting ways than regular prevention education materials. Prevention educators need up-to-date and relatable programming that can be easily adapted to different delivery methods.

This study is important because it identifies the concerns and benefits that were experienced by the prevention educators while delivering SA/DV prevention education during the COVID-19 pandemic. Future researchers should conduct a deeper analysis to fully understand how prevention educators combated the lockdowns, social distancing policies, and other concerns regarding COVID-19.

References

CDC. (2017). Preventing Intimate Partner Violence Across the Lifespan: A Technical Package of Programs, Policies, and Practices. Division of Violence Prevention. https://www.cdc.gov/violenceprevention/pdf/ipv-technicalpackages.pdf

Center for Disease Control and Prevention [CDC]. (2020). Effects of the Dating Matters Comprehensive Prevention Model on Health- and Delinquency-Related Risk Behaviors in Middle School Youth: a Cluster-Randomized Controlled Trial. Prevention Science. file:///C:/Users/vpaf.assistant1/Downloads/cdc_95044_DS11.pdf

Cheung, S.P., Huang, C.C. (2022). Childhood Exposure to Intimate Partner Violence and Teen Dating Violence. *J Fam Viol*. https://doi.org/10.1007/s10896-022-00377-7

Dosil, M., Jaureguizar, J., Bernaras, E., & Sbicigo, J. B. (2020). Teen Dating Violence, Sexism, and Resilience: A Multivariate Analysis. *International Journal of Environmental Research and Public Health*, *17*(8), 2652. https://doi.org/10.3390/ijerph17082652

Eleby, C.J. (2009). The Impact of a Student's Lack of Social Skills on their Academic Skills in High School. https://files.eric.ed.gov/fulltext/ED529283.pdf

Kann, L., McManus, T., Harris, W. A., Shanklin, S. L., Flint, K. H., Hawkins, J. et al. (2016). Youth risk behavior surveillance – United States, 2015. MMWR Surveillance Summaries. Volume 65 (No. SS-6), 1-174.

Williams, N. (2021). Working through COVID-19: 'Zoom' gloom and 'Zoom' fatigue, Occupational Medicine, Volume 71, Issue 3, Page 164, https://doi.org/10.1093/occmed/kqab041

Augmented Omni-Surface for Human-Robot Collaboration Through Visualization and Touching

Edgar Chavez *and*
Hongsheng He, PhD
School of Computing, Wichita State University

Introduction

The relevance of the human-robot interface, also referred to as human-robot teaming, grows as robots operate in proximity to human workers more frequently. Compared to conventional industrial robots that work alone, advanced industrial robots are expected to collaborate with human co-workers. Previous research (Lasota & Shah, 2015) has indicated that with human-robot collaboration, the manufacturing process becomes quicker, more efficient, and less costly.

For gesture-based human-robot teaming interfaces, gesture ambiguity increases as the tasks get complicated, whereas touch interaction is unambiguous and comfortable to use for extended periods (Xiao, Schwarz, Throm, Wilson, & Benko, 2018). The development of commercial RGB-D sensors increase the prospect of converting these ordinary surfaces into touchable and interactive devices (Ntelidakis, Zabulis, Grammenos, & Koutlemanis, 2015). Therefore, a human-robot teaming method based on touching can benefit human-robot teaming. For this purpose, this paper proposes an augmented Omni-surface that can directly interact with robots.

To enable surfaces with interactive touching feedback, previous work has focused on refurbishing existing surfaces by adding other sensors such as acoustic sensors (Harrison & Hudson, 2008). Two difficulties prevent human-robot collaboration with a touching method without refurbishing the current environments: touch detection and surfacing fitting. A conventional image processing method (Bhuyan, Neog, & Kar, 2012) can detect fingertips. However, this method is limited by the complexity of the background (Xiao, Hudson, & Harrison, 2016). A touch detection method equipped with depth cameras is (Xiao et al., 2016) suitable for flat surfaces. However, the working place for human-robot teaming contains not only flat surfaces but also curvy surfaces such as the carbine of a plane.

In this paper, we propose a method that enhances human-robot teaming by directly interacting with robots on the surface of the working space. To adapt to different working environments, the touch detection method can enable humans to interact with robots by touch in different human-robot teaming environments such as flat, curvy, convex, and concave surfaces with a single commercial RGB-D camera. Fingertips are detected with a convolutional neural network (CNN), and touch is detected based on the RGB-D sensor.

Augmented Omni-Surface

Touch detection is essential to enable augmented Omni-surface for human-robot teaming. Augmented Omni-surfaces can superimpose mutual understanding between humans and robots on the surfaces of working space. This study contains two parts: surface fitting and touch detection. The RGB-D sensor captures an image containing a user's hand, which will be the input for the fingertip's detection and surface modeling module.

Arbitrary Surface Fitting

To fit the surface based on the collected depth scans, we assume the targeted surface is visible to the RGB-D camera. We then proceed to collect random pixels from the targeted surface. To fit the surface in a 3D space, we need to transform 2D pixel coordinates to 3D world coordinates by using the intrinsic parameters of the image from the RGB-D sensor. With these random pixel coordinates, we can perform deprojection to calculate the depth of our random pixel coordinates. In our proposed method, we use global surface approximation to create an approximation of the targeted surface. With our approximate surface, we extract any curves that may exist. This will return any curves that lie on the control point's surface.

Surface Touch Detection

Without installing additional hardware such as touch screens (Kim, Son, Lee, Kim, & Lee, 2013), it is challenging for the system to get feedback from human users. The proposed system is designed to detect touch by an RGB-D sensor.

To detect fingertips from input images, two problems need to be solved: hand recognition and determining the coordinate of the fingertips. Earlier methods (Lai et al., 2016), isolated the hand regions from the acquired images using features such as color, depth, and contours. To obtain the coordinates of fingertips, the previous method (Liao, Zhou, Zhou, & Liang, 2012), employed a convex model that can model the endpoints of the extracted hand region, however, this doesn't always find optimal results and is computationally costly.

In this study, we formulate the problem of recognizing the hand and detecting the fingertips as a unified problem that combines classification and regression by implementing a deep learning model. To detect fingertips, we first detect the hand with 16 layers of visual geometry group (VGG) structures (Simonyan & Zisserman, 2014). Then, we recognize fingertips with a deep learning model that includes convolution layers, flatten layers, and coordinate layers. The fingertip detection model input is an image containing a single hand, and the model's output

is the recognized fingers and their respective coordinates.

To detect whether the user touched the surface or not, we compute the Euclidean distance between the detected fingertip and the approximated surface world coordinate frame. We then find the distance between the detected fingertips and approximated surface points. Lastly, we find a minimum distance to compare to the depth with the average thickness of a human's finger to determine if fingertips are touching the surface.

Experiment

To evaluate the performance of the method to augment Omni-surfaces, we executed the proposed system in different scenarios to investigate the generality of the method. To investigate performance, we computed the accuracy of our touch detection method. We also evaluated user's satisfaction.

Performance of Finger Touching

We tested the augmented Omni-surfaces method in different scenarios, such as smooth and curved surfaces. These scenarios cover different shapes and materials of the surface. Our results conclude that the augmented Omni-surfaces method is reliable in practical usage. Two faults were detected in this experiment. When the working surface is too small, depth collections include more noise than desired points. One solution would be to decrease the area of the points being collected and increase the number of points collected.

User Satisfaction

To evaluate user satisfaction with augmented Omni-surface interaction, we designed and distributed a questionnaire to 20 participants that measured four evaluation criteria: correctness, ambiguity, effectiveness, and complexity. We also assigned the weight for each criterion to compute the final score for each perspective. 1) Correctness is defined as whether the user can instruct the robot with the proposed interaction method; 2) Ambiguity is defined as whether the user can precisely give the robot's instructions; 3) Compared with other interaction methods such as programming or physical interaction with buttons, the designed interaction is effective; 4) Compared with other interaction methods, the designed interaction is complicated. Feedback from the questionnaires indicate users are satisfied with the proposed interaction method.

Conclusion

A method of touch detection for human-robot teaming has been proposed based on RGB-D sensing to detect a touch on arbitrary surfaces to enhance human-robot teaming. The proposed interface demonstrated improved user acceptance of traditional interaction methods according to the results of user satisfaction questionnaires.

References

Bhuyan, M., Neog, D. R., & Kar, M. K. (2012). Fingertip detection for hand pose recognition. *International Journal on Computer Science and Engineering, 4*(3), 501.

Harrison, C., & Hudson, S. E. (2008). *Scratch Input: Creating Large, Inexpensive, Unpowered, and Mobile Finger Input Surfaces.* Paper presented at the Proceedings of the 21st Annual ACM Symposium on User Interface Software and Technology, New York, NY, USA.

Kim, S., Son, J., Lee, G., Kim, H., & Lee, W. (2013). *TapBoard: making a touch screen keyboard more touchable.* Paper presented at the Proceedings of the SIGCHI Conference on Human Factors in Computing Systems.

Lai, Z., Yao, Z., Wang, C., Liang, H., Chen, H., & Xia, W. (2016). *Fingertips detection and hand gesture recognition based on discrete curve evolution with a kinect sensor.* Paper presented at the 2016 Visual Communications and Image Processing (VCIP).

Lasota, P. A., & Shah, J. A. (2015). Analyzing the effects of human-aware motion planning on close-proximity human--robot collaboration. *Human factors, 57*(1), 21-33.

Liao, Y., Zhou, Y., Zhou, H., & Liang, Z. (2012). *Fingertips detection algorithm based on skin colour filtering and distance transformation.* Paper presented at the 2012 12th International Conference on Quality Software.

Ntelidakis, A., Zabulis, X., Grammenos, D., & Koutlemanis, P. (2015). *Lateral touch detection and localization for interactive, augmented planar surfaces.* Paper presented at the International symposium on visual computing.

Simonyan, K., & Zisserman, A. J. a. p. a. (2014). Very deep convolutional networks for large-scale i mage recognition.

Xiao, R., Hudson, S., & Harrison, C. (2016). *Direct: Making touch tracking on ordinary surfaces practical with hybrid depth-infrared sensing.* Paper presented at the Proceedings of the 2016 ACM International Conference on Interactive Surfaces and Spaces.

Xiao, R., Schwarz, J., Throm, N., Wilson, A. D., & Benko, H. (2018). MRTouch: Adding Touch Input to Head-Mounted Mixed Reality. *IEEE Transactions on Visualization and Computer Graphics, 24*(4), 1653-1660.

Quantum Neural Network Training of a Repeater Node

Jackson Dahn *and*
Elizabeth Behrman, PhD

Department of Mathematics & Statistics, Wichita State University

Introduction

One major issue in current quantum computing research is the development of algorithms that fully leverage quantum phenomena to produce a computational advantage[1]. Efficient and physically attainable algorithms for quantum computing have proven difficult to design. Our approach to this problem is to eliminate the need for humans to design the algorithm and allow a neural network, called a quantum neural network (QNN), to construct the algorithm. Quantum neural networks are capable of producing robust and scalable control algorithms for quantum computers[2, 3]. This project aims to demonstrate that these properties transfer well to the control of a quantum repeater node, a linear operation consisting of swapping the states of a set of input qubits and a corresponding set of output qubits. A quantum repeater can be constructed as a system that initializes output qubits and receives input qubits [4]. The repeater then swaps each input state with its corresponding state, where is output from the system and is stored in the repeater and remains entangled with. The repeater essentially functions as a signal amplifier, however, because the incoming signal cannot be copied, the input and output signals are swapped instead. When the outgoing qubit is measured, the input signal collapses with the measurement. The output signal initialized inside the repeater can be arbitrary, and thus can generally be initialized to a standard state that is easy to produce.

The operations of a repeater are fully contained in a swap gate. The swap gate of a repeater can be represented as a single unitary operation. This operation, or gate, is what is trained by the QNN.

Methodology

To construct the quantum repeater system, we first construct the form of the Hamiltonian acting on the system as where are the Pauli spin matrices, and are the tunneling, bias, and coupling coefficients for each qubit (or qubit pair in the case of ζ). The qubits being acted on are represented in their density matrix form . The system then evolves in time according to the Schrödinger equation . This representation of the system has proven complementary to the training of a QNN[1, 2] because of the similarities between the quantum system and a neural network. The parameters K, ε, and ζ were broken apart into coefficients of a Fourier sum at each timestep, and these parameters were the weights trained by the neural net. The Hamiltonian was then precompiled, and the system evolved through time. Error E was then calculated at the final time applied to a Levenberg-Marquardt weight update rule for each training epoch. To train and test the system, we first trained the system in a noiseless environment, and then added depolarizing noise[5] for further training and testing.

Results

To first establish a baseline for training effectiveness, a set of two qubits was trained to sufficient error E, and those parameters were transferred to the four, six, and eight qubit cases. The baseline results are summarized in Table 1 for a standardized testing set consisting of different pairs of coupled qubits with a sweep of the relative phase between them.

n_{qubits}	Trained rms ()
2	1.818
4	4.454
6	4.235
8	5.286

Table 1 noiseless trained rms values

With a fidelity very close to unity, it is clear that the QNN is able to reproduce the noiseless SWAP gate effectively for any number of qubits. While K and ε are similar functions of time for all qubits, here it is important to note that in the noiseless case, the non-pairwise terms —that is coupling not between a pair of qubits being swapped— are essentially trained to zero. With the baseline established, we can now look at the results for the noisy case. In each case, the noiseless parameters were used as a starting point and further trained with the noisy system, with the major changes to the trained parameters being made in the non-pairwise ζ terms. Investigation is still ongoing and finalized results were not available for inclusion in this report. However, an overview of current progress is given. Using a depolarizing noise model with a λ on the order of 10^{-3}-10^{-6}, the root mean square (rms) of the system is initially rising to about – two orders of magnitude larger than the noiseless values. This is expected, however, after about 30 training epochs the error is lowering at least one order of magnitude on average. The ζ values are again the parameter changing the most, as the QNN builds a way to use the non-pairwise terms to add robustness of the system. Current ζ values for the 4 qubit system are shown in Figure 1.

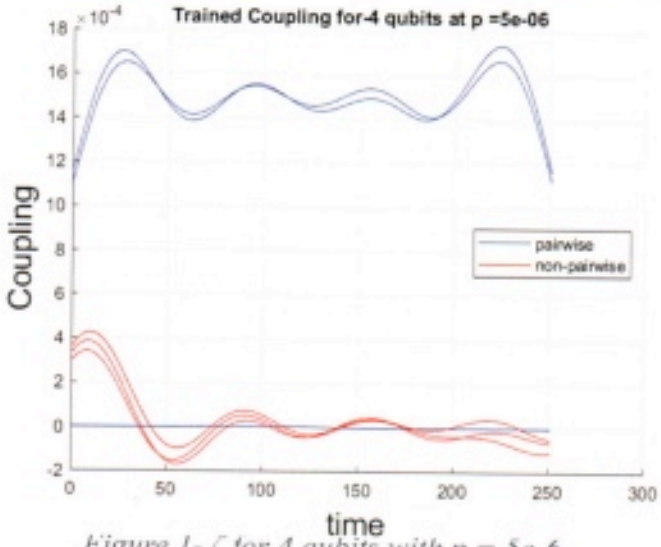

Figure 1- ζ for 4 qubits with p = 5e-6

Conclusion and Further Discussion

The following conclusions of the project can be drawn from partial results, and other trends can be discussed. In short, through the noiseless case, the QNN was able to demonstrate scalability. However, the system has not yet demonstrated robustness through the introduction of noise. Current progress is trending toward this result, however, there is more work to be done to test the limits of the robustness.

As previously discussed, this simulation is offline learning. To be able to backpropagate the error through time, we must know the state of the system at each time step. This is clearly not possible as any measurement of the system would cause it to collapse. Thus, real hardware implementation would not be able to use this type of learning. Other control problems have run into this issue with classical systems, and a common approach is to construct a model of the system for offline learning and perform all the training in simulation. Once the model is sufficiently trained, the parameters can be transferred to the online system and, if needed, further trained by some potential method not needing access to the state of the system at intermediate times. To construct the best possible model of the system for offline learning, many hardware-specific parameters must be known. Examples would be internal biases, relaxation and decoherence times, and actuation parameters. This was something we chose not to do in this project to produce a more general result. However, the logical progression of this research would be the implementation of this approach on actual hardware, ideally on a large variety of hardware.

Even without hardware testing, these results are promising for the problem of the quantum repeater. Quantum repeaters will be the backbone of quantum networks and will need to be able to process large numbers of qubits with high fidelity. The QNN presented here allows the ability to trivially copy itself ad infinitum to handle the desired number of qubits. Additionally with this scheme, it was also shown noise can be dealt with purely by the coupling of the qubits, meaning the QNN can be generalized by training of a small number of qubits, and error correction can be handled by training the coupling coefficients.[1]

References

E. C. Behrman, J. E. Steck, P. Kumar and K. A. Walsh, (2008), pp. arXiv:0808.1558.

N. H. Nguyen, E. C. Behrman and J. E. Steck, (2016), pp. arXiv:1612.07593.

N. L. Thompson, N. H. Nguyen, E. C. Behrman and J. E. Steck, (2019), pp. arXiv:1902.07754.

S.-H. Wei, B. Jing, X.-Y. Zhang, J.-Y. Liao, C.-Z. Yuan, B.-Y. Fan, C. Lyu, D.-L. Zhou, Y. Wang, G.-W. Deng, H.-Z. Song, D. Oblak, G.-C. Guo and Q. Zhou, (2022), pp. arXiv:2201.04802.

M. A. Nielsen and I. L. Chuang, *Quantum computation and quantum information.* (Cambridge University Press, Cambridge ; New York, 2000).

Deflocculation: The Effects of Calgon on Ancient Starch Recovery

Savanna Gann *and*
Crystal Dozier, PhD
Department of Anthropology, Wichita State University

Introduction

Extraction Techniques

While commonly accepted archaeobotanical extraction techniques have been established among dedicated ancient starch researchers (Torrence and Therin 2006; Cuthrell and Murch 2016), studies continue to test the efficiency, cost-effectiveness, and accuracy of extraction techniques (Horrocks 2005; Korstanje 2006; Louderback et al. 2015). In the process of deflocculation, sediments that contain ancient starch residues are soaked in a strongly charged ion solution, such as Calgon (sodium hexametaphosphate) or sodium polytungstate, to release microbotanical remains from clay particle aggregates (Cuthrell and Murch 2016). Exposing clay-rich sediments to the process of chemical deflocculation causes the clay particles to bond to the ions, neutralizing the electrical charges that cause the particles to attract one another and form aggregates. In disaggregating the sediment particles, microbotanical residues are released and separated from the sediment sample through size fractionation.

Chemical deflocculation is a common technique among ancient starch researchers and has been well documented in numerous studies and experiments. Torrence and Therin (2006) examined multiple chemical solutions used as deflocculants to find the ideal method for extracting starch from sediments. The results showed that sodium polytungstate does not appear to have a corrosive effect on starch at normal room temperature while caesium chloride and sodium hexametaphosphate both damaged starch morphology and quantity. Given these results, Torrence and Therin suggest that the potentially destructive effects of chemical deflocculation be balanced against the benefits of the process. However, other studies, including that of Cuthrell and Murch (2016), have utilized deflocculation with significantly less loss to starch samples and less damage to granule morphology. In the case of Cuthrell and Murch, exposure to a 4% sodium hexametaphosphate solution for 24 hours did not consistently cause detectable changes in the morphology of potato or wheat starches. Conflicting

conclusions regarding the deleterious effects of deflocculation widen the gap in ancient starch literature and must be addressed further.

Use of Calgon

Calgon, or sodium hexametaphosphate, is a rapid and inexpensive way to clean artifacts that have recently been recovered from an extraction site. Calgon baths have been used in the deflocculation stage of starch analysis for decades, most commonly with a 5% solution. While Calgon is still commonly used in laboratory and field settings, some research within the literature suggests that the deflocculant causes granule damage, changes in morphology, and reduction in starch quantity. The commonly accepted 5% solution of sodium hexametaphosphate has caused "no noticeable" damage in some studies while also causing "detectable" and "significant" damage in others (Cuthrell and Murch 2016; Neumann and Sanford 1998); the discrepancies between these results will be further explored in this study.

Methods

Note on Previous and Current Studies

The following study is the continuation of a previous experiment (Gann and Dozier 2021). The original *Starch in Deflocculation* produced limited preliminary results because not all created samples were counted due to time constraints; only the rinse, 60-minute, and 24-hour samples were included in the data collection and subsequent results. Following initial publication, the remaining 5-minute, 10-minute, 30-minute, and 120-minute sample slides were counted but produced inconclusive results due to incredibly high starch presence and uneven starch granule distribution. As such, the experiment was repeated with modified methods to limit starch density and increase accuracy.

Methodology

Ten *Lycopodium* tracer spore tablets, each containing 19,855 spores, were dissolved in a 10% hydrochloric acid solution (%v/v). The dissolved *Lycopodium* tablets were then centrifuged at 3300 rpm for 3 minutes, decanted, and vortexed. The Calgon-Starch solution was prepared by mixing 0.2 g of commercial cornstarch (Argo, Inc) with 100 ml of a 5% Calgon solution (%w/v). The *Lycopodium* tracer spores were added to the Calgon-Starch solution, signaling the start of the timed soakings. Six 1 ml samples of the Calgon-Starch-*Lycopodium* solution were then placed in six separate test tubes and mixed with 4 ml of distilled water, creating a solution of 0.0004 g of starch per 1 ml of Calgon. Each test tube was centrifuged at 3300 rpm for 3 minutes at its respective timestamp – rinse, 10-minute, 30-minute, 60-minute (1-hour), 120-minute (2-hour), and 1440-minute (24-hour) – then decanted and vortexed. Slides were prepared following a 1-to-1 ratio of the sample solution and glycerin.

Slides were analyzed under brightfield and polarized light microscopy with an OMAX Lab LED binocular microscope at 200-600x magnification. Starch and *Lycopodium* spores were counted simultaneously, with 100 *Lycopodium* spores counted in each sample, to understand the ratio of starch to control spores over-soaking time in Calgon. Data was collected manually with the human eye and a mechanical counter.

Results

Results indicate that starch recovery can decrease by almost half when soaked in Calgon for a 24-hour period. Table 1 summarizes the results from each of the samples with their respective starch, *Lycopodium*, and ratio numbers. Figure 1 depicts the change in Starch-*Lycopodium* ratio over time.

Table 1

Time (min)	Starch Quantity	*Lycopodium* Quantity	Starch-*Lycopodium* Ratio
Rinse	8,320	100	83.2
10	7,739	100	77.39
30	10,538	100	105.38
60	7,342	100	73.42
120	5,186	100	51.86
1440	4,963	100	49.63

Figure 1

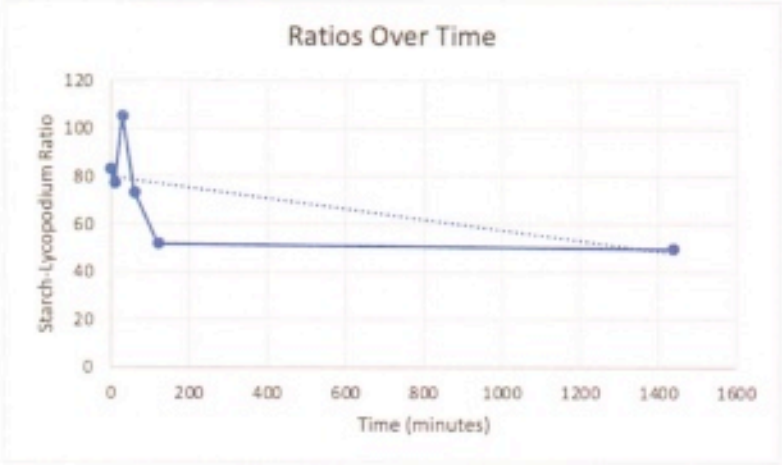

Discussion

The amount of time in which starch is left to soak in Calgon affects recovery. Results from the experiment show that starch sample sizes may decrease by nearly half when left in Calgon for 24 hours, an amount of time common for deflocculation in the field of archaeology. The significant decrease in starch recovery from the rinse to the 60-minute samples suggests that ancient starch researchers who hoped to extract as many starch granules as possible should soak source materials in Calgon for less than 1 hour. The continual decrease from the 60-minute to the 1,440-minute further suggests that prior deflocculation with Calgon for the standard 24-hour period has harmed starch recovery in previous experiments and studies.

Starch density in this experiment was moderately high, with granules unevenly dispersed across slides. Also, the study relied on a human-based counting system. As such, granule abundance and human error may have impacted data collection. To further understand the effects of Calgon on starch recovery, additional studies should be conducted with more controlled measures of starch distribution and more efficient data collection methods.

Conclusion

Deflocculation with Calgon has previously proven to be an inexpensive and efficient way of cleaning specimens recovered from archaeological sites. However, experiment results suggest that soaking artifacts or sediment samples in Calgon for 1 hour to 24 hours can significantly reduce starch recovery, implying a potential reduction of starch quantity in previous ancient starch research. Ancient starch researchers intending to extract starch granules efficiently and with minimal damage should soak source materials in Calgon for less than 1 hour.

References

Cuthrell, Rob Q., and Loren V. Murch. 2016. "Archaeological Laboratory Extraction Procedures and Starch Degradation: Effects of Sonication, Deflocculation, and Hydrochloric Acid on Starch Granule Morphology." *Journal of Archaeological Science: Reports* 9 (October): 695-704. https://doi.org/10.1016/j.jasrep.2016.08.037.

Gann, S. and Dozier, C. Pending Publication. "Starch in Deflocculation: The Effects of Calgon on Ancient Starch Recovery." *McNair Scholars Program Journal of Research Reports, 26*

Horrocks, Mark. 2005. "A Combined Procedure for Recovering Phytoliths and Starch Residues from Soils, Sedimentary Deposits, and Similar Materials." *Journal of Archaeological Science* 32, 1169-1175. https://doi.org/10.1016/j.jas.2005.02.014.

Korstanje, Alejandra M. 2006. "Designing a Protocol for the Simultaneous Recovery of Multiple Microfossils." In *Ancient Starch Research*, edited by Huw Barton and Robin Torrence, 162-163. Walnut Creek: Left Coast Press.

Louderback, Lisbeth A., Judith Field, and Joel C. Janetski. 2015. "Curation Practices and Extraction Methods in Relation to Starch Grain Yields from Ground Stone Artifacts." *Journal of Archaeological Science: Reports* 4, 535-540. https://doi.org/10.1016/j.jasrep.2015.10.011.

Neumann, Thomas W., and Robert M. Sanford. 1998. "Cleaning Artifacts with Calgon." *American Antiquity* 63(1) (January): 157-160. https://doi.org/10.2307/2694782.

Torrence, Robin, and Michael Therin. 2006. "Experiments for Testing Starch Extraction Techniques." In *Ancient Starch Research*, edited by Huw Barton and Robin Torrence, 156-158. Walnut Creek: Left Coast Press.

Creating Digital Twins of Cells using Computational Machine Learning

Julie Gonzalez-Morales *and*
David Long, PhD

Biomedical Engineering Department, Wichita State University

Introduction

The human body has an abundance of endothelial cells that comprise a monolayer known as the endothelium. This cell layer runs all over the body but is mostly focused and tethered to the cardiovascular system. Its functions include moving cells and nutrients throughout the body and maintaining good blood flow. The endothelium is highly active in terms of its functions and can be thought of as an input/output system [1]. Endothelial cells communicate in an interesting way. The stress or conditions that could activate one cell might not activate another, and thus it is crucial to study endothelial cells as a whole rather than independently [1]. It is understood that there is a relationship between cell shape or cell morphology and physiological responses [2]. Each endothelial cell has a limited response to stimuli or force, and a greater response to the endothelium [3], but the mechanism for cell communication and response is not yet certain. Altering the wall sheer stress for a prolonged period of time can alter the cell's gene and protein regulation, leading to vascular changes [4]. By altering a part of the system and measuring its response, we can begin to understand how the altered part affects the system. The purpose of this project is to develop a machine learning (ML) algorithm that can predict the internal structures of a cell, (i.e., nucleus, focal adhesions, f-actin, etc.) with only the shape of the membrane. By developing digital twins, both live-cell signaling dynamics and subcellular morphology can be predicted.

Methods

This study is an extension from a previous study and followed closely to methods indicated in "A Machine Learning Framework to Predict Subcellular Morphology of Endothelial Cells for Digital Twin Generation" [5]. Previous work included the staining, imaging, segmentation, and prediction of the membrane, nucleus, and focal adhesions. The method will be extended to encompass f-actin which will be stained and imaged using Phalloidin.

Cell Culture and Media

The process of cell culture and media was as follows:

> "Human Microvascular Endothelial cells (HMEC-1, #CRL-3243, ATCC, Manassas, VA) were maintained in complete growth media. Complete growth media consisted of MCDB 131 media (#10372019, Gibco, Grand Island, NY) supplemented with 2 mM L-glutamine (#25030081, Thermo Fisher Scientific), 10% (v/v) FBS (#15000044, Thermo Fisher Scientific) and penicillin/streptomycin (100 U/ml and 100 µg/ml concentration, respectively). Cells were seeded at a density of 10,000 cells/cm2 onto fibronectin-coated glass coverslips (#CS-25R17, thickness 1.5, Warner Instruments, Hamden CT) (fibronectin, 20 µg/ml, #33016-015, Thermo Fisher Scientific) mounted in 6-well plates. The cells were grown to confluence in a humidified environment at 37°C with 5% CO2." [5]

Immunofluorescence Labeling

Three stains were used to label three different structures. Wheat Germ Agglutinin (WGA) was used for the plasma membrane of live cells. Hoescht 33258 was used for the nucleus. F-actin will be stained as well using Phalloidin according to manufacture protocol. The immunofluorescent labeling done on the cells was as follows for the nucleus and membrane:

> "Once the cells reached confluence, the plasma membrane of live cells were stained with Wheat Germ Agglutinin (WGA) (CF633, Biotium, Fremont, CA). Cells were washed twice in Hank's Balanced Salt Solution (HBSS, #14025076, Thermo Fisher Scientific), then incubated with WGA (5 µg/ml) for 30 minutes at 37°C, then washed twice in HBSS. Next, the cells were simultaneously fixed (4% (w/v) paraformaldehyde (PFA) in PBS) and permeabilized in Triton X-100 (0.5% (v/v), 5 min, #T9284, Sigma-Aldrich). Then post-fixed in 4% (w/v) PFA in PBS, followed by PBS wash (3 × 5 min). To image the nucleus, cells were stained with Hoechst 33258 (1:1000, #116M4139V, Sigma-Aldrich). A blocking solution comprised of goat serum (1:20, #G9023, Sigma-Aldrich), 0.1% Triton X-100, and 0.3M glycine in 0.1% (w/v) BSA was added to cells for 30 minutes." [5]

Microscopy and Imaging

It is important to acquire images with the same properties (i.e stacks with certain number of slices, size, etc) so the computational segmenting is simpler. The cells were imaged using the following method and settings:

> "A Leica TCS SP5 confocal microscope with a 63×/1.40 NA oil immersion lens was used to image the monolayer. UV 405 nm (nucleus), UV 488 nm (FA sites), and a HeNe 633 nm (membrane) lasers were used to sequentially excite samples. Images were acquired at 2048 pixels × 2048 pixels, with an x-y spatial resolution of 0.087 μm/pixel and z spatial resolution within the range of 0.1-0.15 μm/slice for different imaging sessions. A total of 8 fields of view (i.e., 8 image stacks) were acquired from cells belonging to all well plates." [5]

Image Processing

The image processing was done through napari, a fast, interactive, multi-dimensional image viewer for Python. It is designed for browsing, annotating, and analyzing large multi-dimensional images. The original "raw" image and the annotated "ground truth" image 2048 x 2048 pixels were spilt into images of size 256 x 256 pixels. This was done to decrease the training time. For each stack, a slice with max projection of each pixel in the 3D stack was found using code passed down from a collaboration with Dr. Chen, a data scientist at the Leibniz Institute for Analytical Sciences – ISAS. Once the max projection has been determined, a new 2D image is generated and split into 256 x 256 pixels and annotated with a mask created using napari and then incorporated into the training algorithm. These split images were then incorporated into the "training algorithm." After completion of the training algorithm, an image that had not been seen by the training algorithm was used to "test" the accuracy of the training. This process continued until minimal manual annotation was needed.

Machine Learning Training

Training a machine learning (ML) algorithm to automate cell segmentation is done to ensure consistent results of cell segmentation for each input and to minimize discrepancies between manual segmentation. From the automated cell segmentation, these are then fed into train another ML that will predict the actual digital twin.

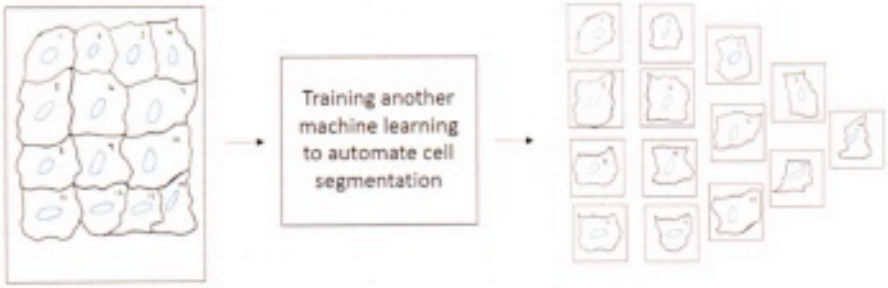

Figure 4.1: The general process of the ML training to automate the cell segmentation process.

Figure 4.2: Representative process for ML of digital twin. Only the nucleus is labeled for representative purposes. All structures will be be stained and imaged to train the ML which are nucleus, membrane, f-actin, etc.

Figure 4.3: Multicell image with only the membrane stained imaged and automatically segmented are then turned into single cells images. Cell images are fed into the ML that has been trained to predict the ML digital twin. A prediction is generated with the structures (f-actin, focal adhesion, nucleus…etc) an a digital twin of the cell is produced.

Prediction Validation

When a digital twin prediction has been made, the results will need to be compared to the ground truth to determine how accurate the prediction is.

Results

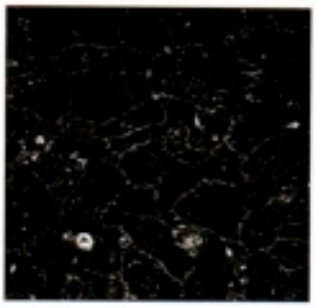

Figure 5.1: Raw image of endothelial monolayer.

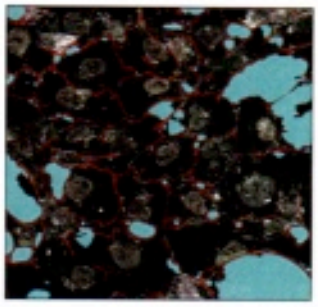

Figure 5.2: Automatic segmentation produced form the ML of the raw image.

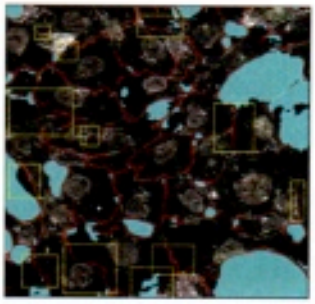

Figure 5.3: Manual segmentation produced from the raw image with differences highlighted in yellow boxes from the ML segmentation.

Results for the prediction of f-actin have not been gathered yet due to the unanticipated heavy focus on the segmentation portion of the project. Manual segmentation can vary between researchers and requires extra time, highlighting the need for automatic segmentation. The ML network has been set up and is currently being trained to produce better-quality automatic segmentation. Overall, the importance of this digital twin is that detailed morphology can be acquired from the cell without having to physically label all the structures of a cell. Although, it is possible to manually stain an image the structures needed, a digital twin would save time and resources. As seen in images 5.1 to 5.3, the differences are highlighted between the segmentation produced from the ML and the manual segmentation. As the ML is more heavily trained, the ML segmentations should improve.

Conclusion

Limitations

The prediction of f-actin for the cells has not been completed due to unanticipated heavy focus on the segmentation portion. The heavy focus for automated segmentation resulted from issues with manual segmentation, namely differences between each manual segmentation, time costliness and less quality predictions. For this reason, we are partnering with Dr. Jianxu Chen and Justin Sonneck from the Leibniz Institute for Analytical Sciences. They have developed the code that will produce the automatic segmentation. The time costliness to train the ML for the segmentation predictions and the digital twin will in the long run be more resource friendly. Automatic segmentation is a crucial step that will produce better quality predictions. Another limitation is determining the threshold for when the ML for both the segmentation and digital twin have been trained enough to be able to predict accurately.

Future Research

Future research might identify and extend these methods to new structures so they can be predicted accurately. Once the digital twin model has been established and trained, it can then be used for a variety of things including looking at live cell signaling dynamics and morphology with limited resources.

References

W. C. Aird, "Spatial and temporal dynamics of the endothelium," (in eng), *J Thromb Haemost*, vol. 3, no. 7, pp. 1392-406, Jul 2005, doi: 10.1111/j.1538-7836.2005.01328.x.

A. S. Vasilevich *et al.*, "On the correlation between material-induced cell shape and phenotypical response of human mesenchymal stem cells," (in eng), *Sci Rep,* vol. 10, no. 1, p. 18988, Nov 4 2020, doi: 10.1038/s41598-020-76019-z.

J. G. McCarron, M. D. Lee, and C. Wilson, "The Endothelium Solves Problems That Endothelial Cells Do Not Know Exist," (in eng), *Trends Pharmacol* Sci, vol. 38, no. 4, pp. 322-338, 2017, doi: 10.1016/j.tips.2017.01.008.

P. F. Davies, "Flow-mediated endothelial mechanotransduction," (in eng), *Physiol Rev,* vol. 75, no. 3, pp. 519-60, Jul 1995, doi: 10.1152/physrev.1995.75.3.519.

M. Contreras, R. W. Hafenstine, W. Bachman, and D. S. Long, "A Machine Learning Framework to Predict Subcellular Morphology of Endothelial Cells for Digital Twin Generation," bioRxiv, p. 2022.03.21.485159, 2022, doi: 10.1101/2022.03.21.485159.

Quiviran Vessel Analysis

Robbyn Mckellop *and*
Donald Blakeslee, PhD
Department of Anthropology, Wichita State University

Introduction

The Great Bend aspect is an archeological classification of sites that includes artifacts from the Wichita People, an indigenous group that lived in the Great Bend area. The sites of the Great Bend aspect are located in McPherson, Cowley, Marion, and Rice Counties in the state of Kansas. Little is known regarding the Wichita People or the time that they lived in the Great Bend area. Present-day research is built largely on the work of archaeologist, Waldo Wedel, who conducted excavations on two of three known village clusters in the area. Through that work, Wedel characterized the Great Bend aspect into two foci: the Little River focus and the Lower Walnut focus. Using McKern's (1939) Midwestern Taxonomic Classification, Wedel defined sites located in McPherson and Rice counties as the Little River Focus and sites located along the Kansas-Oklahoma border as the Lower Walnut Focus (Blakeslee and Hawley 2006; Wedel and Stewart 1959). A third village cluster found in Marion County has produced artifacts that are indicative of migration from McPherson (Zehnder 1998; Rohn and Emerson 1986:51). Wedel affiliated the sites with the Wichita People and estimated the approximate age of the sites. His description of material traits set a baseline for future research in the region (Hoard 2012; Blakeslee and Hawley 2006). Most ethnohistoric discussions surrounding the Wichita People have focused on the Tawakoni, Wichita, Waco, Iscani, and Taovaya bands (Hoard 2012:54).

There is little recorded history of encounters with the Wichita People. The first European to encounter the Wichita People was Francisco Vásquez de Coronado in 1541. (Flint and Flint 2005). While in New Mexico, Coronado was informed of a place named "Quivira" (Flint and Flint 2005). A second, unauthorized expedition by Antonio Gutierrez de Humaña and Francisco Leyba de Bonilla in the 1590s, unfortunately, resulted in the death of almost all in the party. A survivor noted that the party had found a large settlement that extended along a river for several miles with grass thatched houses that were closely spaced together and surrounded by agricultural fields (Craddock and Polt 2013). In 1601, Juan de Oñate led a third expedition to Quivira. Oñate reported finding a "Great Settlement" which was noted to contain between 1,200-2000 houses above the junction of two rivers.

Oñate's soldiers reported that each house held between eight and ten individuals. Reports from one captured native named Miguel suggested that the name of this Great Settlement was "Etzanoa" (Craddock and Polt 2013).

Radiocarbon Dates

Radiocarbon dating is a method that provides objective age estimates for carbon-based materials that originated from living organisms. An age could be estimated by measuring the amount of carbon-14 present in the sample and comparing this against an internationally used reference standard. A team from the Kansas State Historical Society tried to establish a ceramic sequence using vessels associated with radiocarbon samples from cache pits at Etzanoa (Hoard 2012). This proved unsuccessful due to several factors. First, dates were used from scintillation counting which yields large uncertainties. Second, they dated wood charcoal which is problematic because the date will reflect the age of the tree rings in the sample rather than the age of the fire, the age of the fire is important because it helps create an approximate date of when the fire occurred which can create a chronology. This is especially critical because historical evidence shows that the Wichita People used juniper wood for their houses, which have very narrow rings so that a small piece of charcoal is apt to have many rings. The tree rings are important because it is used to compare to an established reference to determine an approximate date as well. If there are a limited number of tree rings it can make it harder, due to environmental factors, to use it reliably as a reference. This adds to the uncertainty regarding how well the radiocarbon date reflects the age of the event. Finally, subsequent work by Wichita State University has shown that many pits contain reverse stratigraphy (Blakeslee 2022). The implication of this is that radiocarbon dates cannot be used to determine the sequences of events during the occupation of Great Bend sites. Since radiocarbon dating has shown to not be an adequate method to create a chronology. Therefore, for this project, I am proposing a method that involves identifying changes through time in the ceramic assemblage by analyzing morphology, handle form, clay properties, manufacturing methods, sooting, carbon patterns, and decoration as a means for determining relative ages.

Methods

Collections

I intend to examine complete and restored cooking vessels from four museums or privately held collections. The Coronado Quivira Museum collection, located in Rice County, holds eight vessels that will be included in this study. Three additional collections contain between one and five vessels, each that I hope to include in our analysis. These include the McPherson Museum collection, a Cowley County Private collection, and the Kansas State Historical Society collection. These collections were chosen based on locality and accessibility.

The pottery will be examined by looking at morphology, handle form, clay properties, manufacturing methods, sooting, carbon patterns, and decoration as a means for determining relative ages. These features will help document variability within and between sites to establish a baseline for examining

change through time. Furthermore, standard measurements will be taken for each vessel. Applicable vessels include complete or restored vessels that retain the profile, base, shoulder, neck, and rim. Temper types, surface treatments, and vessel forms will be recorded. Measurements will be taken for wall thickness and base thickness to identify homogeneity in the technique. Some shape variations may correlate with vessel size rather than time, while other variations will differentiate sites. Stylistic choices such as node placement on handles and rims, punctuates or line and punctate combinations may reflect origins rather than chronology.

Analysis

Variation does not occur solely temporally but may also reflect other factors such as differences between bands and modes of cooking being used. It is important to identify contemporaneous cultural differences to remove them from consideration. Therefore, I propose analyzing the following cultural features: style, shape, iconography, clay properties, manufacturing methods, along with sooting, and carbon patterns.

Discussion

Due to the difficulties dating the Great Bend aspect, reassessing the ceramic assemblage using complete and restored vessels and incorporating seriation techniques may allow us to determine the chronological sequence. These methods are typically used when absolute dating methods like radiocarbon cannot be applied. Using collections from the Coronado Quivira Museum, the McPherson Museum, The Kansas State Historical Society Collection, and a Cowley County Private Collection will be beneficial because the collections derive from separate but contemporaneous communities. One potential limitation to this study is gaining access to an adequate number of vessels. Artifacts from these sites are located throughout the state of Kansas in both private and public collections. Therefore, data collection will involve a significant amount of travel and will require being granted permission to access and document these vessels.

Conclusion

The collections from the Coronado Quivira Museum, the McPherson Museum, the Kansas State Historical Society Collections, and a Cowley County Private Collection require analysis to determine a sequential order of events in the Great Bend aspect. The Great Bend aspect is currently estimated to range between 1425 CE to 1700 CE, which is more than enough time for measurable ceramic change to have occurred. Seriation based on differences in shape, style, iconography, and manufacturing methods will be used. Measurements of the wall, trim, and base thickness will also be used. Stylistic choices that differ between but not within localities will not be used.

References

Blakeslee, Donald J. Personal communication during project proposal. Wichita State University, Wichita, Kansas, 2022.

Blakeslee, Donald J. and Marlin F. Hawley. "The Great Bend Aspect." In Kansas Archaeology, edited by Robert J. Hoard and William E. Banks, 165–79. University Press of Kansas, 2006. http://www.jstor.org/stable/j.ctt1p6qpdm.14.

Craddock, J. R, & Polt, J. H. (2013). Juan de Oñate in Quivira, 1601: the "Relación cierta y verdadera" and the Valverde Interrogatory. UC Berkeley: Research Center for Romance Studies. Retrieved from https://escholarship.org/uc/item/7162z2rp

Flint, Richard, and Shirley CUSHING flint, eds. 2005. Do Expedition, 1539-1542. Dallas: Southern

Hoard, Robert J. (editor) 2012 Archeological Investigations at Arkansas City, Kansas. Kansas Historical Society, Topeka.

Martin Stein, C. "Ceramic Artifacts" In Archaeological Investigations at Arkansas City, Kansas, edited by Robert Hoard, 251-328. Historical Society, Topeka, 2012.

McKern, W. C. "The Midwestern Taxonomic Method as an Aid to Archaeological Culture Study." American Antiquity 4, no. 4 (1939): 301–13. https://doi.org/10.2307/276087.

Rohn, Arthur H., Alice M. Emerson, and Judith A. Malone. Great Bend Sites at Marion, Kansas. Vol. 1 no. 1.; Wichita: Wichita State University, 1984.

Wedel, Waldo R. 1959. "An introduction to Kansas archeology." Bureau of American Ethnology Bulletin. 174:1–723.

Zehnder, Jon P. and Donald J. Blakeslee. 1998. "Relationships between Two Little River Focus Sites in McPherson and Rice Counties of Central Kansas Based on Excavated Lithic Debitage.".

Additive Manufacturing of Ceramic Acoustic Liners for Aircraft Noise Reduction

David Nevarez-Saenz *and*
Bhisham Sharma, PhD

Aerospace Engineering Department, Wichita State University

Introduction

Recent advances in additive manufacturing (AM) allow the fabrication of previously infeasible complex geometries [1]. These improvements have opened new possibilities in the design of open-celled porous sound absorbers for noise reduction applications [2, 3, 4, 5, 6]. Ceramics provide the unique ability to withstand high temperatures and pressures, critical features for engineering structures subjected to extreme environments [7].

Here, our focus is on the AM of ceramic porous absorbers for noise reduction applications. Specifically, our focus is on the use of low-cost, scalable fabrication of ceramic structures with complex internal geometries that provide requisite sound absorption performance. Ceramics are complex bodies, and there are multiple variables to record like material, pressure, and extrusion rate. This indirect process results in dimensional shrinkage and unpredictable mechanical and functional properties due to shrinkage-induced warping and internal flaws [8].

In this paper, we present preliminary results from our efforts on the AM of ceramic porous absorbers. We describe the AM process conducted using a commercially available low-cost clay extrusion printer. We explain the various modifications required to enable the printing of samples with pore sizes necessary for obtaining high sound absorption. The quality of the printed samples is studied using image microscopy, and the effect of the sintering process on the end-part dimensionality is investigated. Then, the sound absorption performance of successful ceramics AM samples is presented. Our results demonstrate the feasibility of using AM to fabricate ceramic absorbers with performance-tailored acoustical properties.

Methods

Materials and Sample Fabrication

In this study, we use an extrusion-based additive method to fabricate acoustic test samples. For this research, we used a commercially available clay printer, Delta WASP 2040 Clay, which comprises three major components: a compressed air tank, a clay tank, and an extruder mechanism controlled via a delta mechanism. The compressed air tank connects to a clay tank and is controlled by a pressure gauge. The compressed air moves a piston within the clay tank and pushes the clay into the extruder; the required pressure magnitude is dependent on the clay pliability. A motor spins the auger within the extruder system and drives the clay down to the nozzle. We modified the extrusion mechanism by replacing the provided auger with a longer auger that allows a layer height of 0.25 mm. Further, the nozzle was replaced by a stainless-steel nozzle with a smaller tip diameter of 0.4 mm.

As part of this work, initial print trials were conducted using porcelain clay provided by the printer manufacturer. The clay was prepared by mixing 1 kg of the clay with water until the desired consistency was achieved. The clay was then wrapped in plastic and allowed to sit for one hour before being placed inside the clay tank.

The printability of the clay is highly dependent on the consistency of the clay mixture; the fabrication of samples with repeatable dimensionality thus requires a repeatable consistency. To this end, a spike test apparatus was designed and used to estimate the clay pliability. The apparatus consists of a 3D printed spike with marked distances and a sleeve within which we place a 10 mm diameter stainless steel rod. The total setup weighs 210 grams and is dropped onto the mixed clay from a height of 100 mm; the clay pliability is then quantified based on the penetration depth. For the clays used here, penetrations above 50 mm were classified as soft clay, between 40 mm and 50 mm were classified as fair clay, and values below 40 mm were classified as hard clay. For the samples printed in this study, the porcelain clay was mixed to achieve a spike penetration depth of 38 mm and extruded at an average pressure of 3.3 bar with a flow rate of 35%. After printing, the samples were allowed to dry for 12 hours before being fired in a Blaauw Products natural gas kiln.

The test samples were modeled using OpenSCAD to a 12.5mm height and 25.4mm width and sliced using Ultimaker Cura. For the acoustic tests, cylindrical samples of 30 mm diameter and 25.4 mm height were designed by modifying the zig-zag infill density in Ultimaker Cura. For the simple cubic design, seven different relative densities were considered: 25.0%, 27.5%, 30.0%, 32.5%, 35.0%, 37.5%, and 40.0%.

In addition to the acoustic test samples, a cube sample with line separations of 2 mm was printed to investigate the effect of print parameters on the dimensional accuracy of the samples. For all samples tested, the following main settings were used in the slicer software: layer height of 0.25 mm, nozzle size of 0.40 mm, print speed of 20 mm/s, retraction enabled, initial distance from plate board of 0.2 mm, and z-hop when retracted.

Acoustic Absorption Testing

The normal incidence sound absorption coefficient for the cylindrical samples was measured using the two-microphone impedance tube method, as described in the ASTM E1050-19. The test samples were placed in the sample holder section with a rigid background. The incident sound pressure level, as measured at the reference microphone, was maintained at 90 dB. The tube diameter and microphone spacing provide a plane wave test frequency range of 600 – 6100 Hz.

Results and Discussion

Sample Print Quality Microscope

Microscope images of the printed samples before and after firing were taken. All samples are printed using a nozzle diameter of 0.4 mm, while the spacings between the neighboring lines are 2 mm. For all samples, the horizontal spacing and the line thicknesses differ from the as-modeled dimensions. The line thicknesses, nominally 0.4 mm, are closer to an average of 0.53 mm for all samples before firing, indicating an over extrusion of the clay. This over extrusion results in lower than intended spacings in the extruded samples. As expected, post-firing, the samples shrink and result in reduced line thicknesses than the pre-firing samples. While shrinkage is typically undesirable, for acoustic applications requiring smaller pore sizes, this shrinkage could be advantageous and could allow the printing of samples with pore sizes less than those otherwise achievable using typical nozzle dimensions. Further work quantifying the relationship between the material, print process, and dimensional parameters is ongoing.

3.2. Sound Absorption Behavior

The measured sound absorption curves for the 3D printed samples are shown in Figure 1. Overall, the dimensionality of the printed samples is less than desirable. All samples were printed to fit the 30 mm, sample holders by appropriately adjusting the as-designed outer diameter to compensate for the shrinkage occurring during the firing stage.

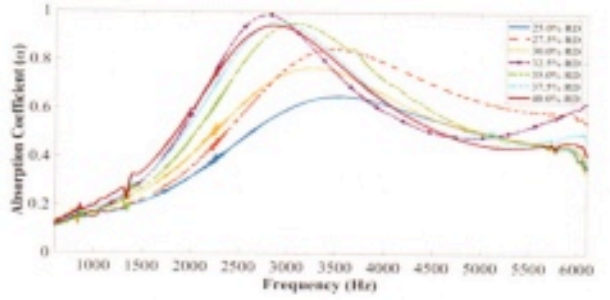

Figure 1. Measured normal incidence sound absorption coefficients for simple cubic samples with 25.0%, 27.5%, 30.0%, 32.5%, 35.0%, 37.5%, and 40.0% relative densities.

The inset pictures show the printed test samples. The absorption coefficients for all the tested samples show a behavior typical of rigid porous absorbers: the absorption initially increases, achieving a maximum absorption value at a frequency corresponding to the quarter-wavelength resonance, before decreasing to a trough and then gradually increasing again.

It should be noted that these absorption values are significantly higher than those observed for equivalent samples printed using polymeric additive manufacturing techniques. This discrepancy is possibly due to the reduction in pore size from the post-sintering shrinkage and the overall poor quality of the printed samples.

Conclusion

In this paper, we presented the preliminary results from our efforts to fabricate ceramic sound absorbers with complex internal pore geometries using AM. A low-cost, commercially available clay extrusion printer was modified to enable the printing of ceramic structures with high dimensional resolutions. While the modifications improved the quality of the samples, issues stemming from over-extrusion and post-sintering material shrinkage remain. Normal incidence impedance tube tests carried out on successful prints show that ceramic AM porous absorbers can provide significantly high sound absorption coefficients at frequencies below 3000 Hz. Current work is focused on further improving the print quality by systematically quantifying the effect of a clay composition, print process settings, and firing schedule on the end-part quality and dimensionality.

References

K. V. Wong and A. Hernandez, "A review of additive manufacturing", International scholarly research notices 2012 (2012).

W. Johnston and B. Sharma, "Additive manufacturing of fibrous sound absorbers", Additive Manufacturing 41, 101984 (2021).

B. Wojciechowski, K. Wetter, C. Cheepa and B. Sharma, "Acoustic properties of 3D printed bulk absorbers with novel surface topologies", Institute of Noise Control Engineering, Vol. 260, pp. 565-572.

F. Setaki, M. Tenpierik, M. Turrin and A. van Timmeren, "Acoustic absorbers by additive manufacturing", Building and Environment 72, 188-200 (2014).

E. R. Fotsing, A. Dubourg, A. Ross and J. Mardjono, "Acoustic properties of periodic microstructures obtained by additive manufacturing", Applied Acoustics 148, 322-331 (2019).

T. G. Zieliński, K. C. Opiela, P. Pawłowski, N. Dauchez, T. Boutin, J. Kennedy, D. Trimble, H. Rice, B. Van Damme and G. Hannema, "Reproducibility of sound-absorbing periodic porous materials using additive manufacturing technologies: Round robin study", Additive Manufacturing 36, 101564 (2020).

W. D. Kingery, H. K. Bowen and D. R. Uhlmann, Introduction to ceramics, John wiley & sons, 1976.

J. Deckers, J. Vleugels and J.-P. Kruth, "Additive manufacturing of ceramics: a review", Journal of Ceramic Science and Technology 5(4), 245-260 (2014).

Assessment of Upper-Limb Task and Joint-Based Exoskeletons for Rehabilitation

Clarissa Rincon *and*
Yimesker Yihun, PhD
Mechanical Engineering Department, Wichita State University

Introduction

Exoskeletons and other robotic devices have been used to assist and automate rehabilitation exercises. As new exoskeleton designs arise, so does the need to assess these devices to ensure patient safety and efficiency. Common challenges in the design process include achieving proper alignment and fitting the robotic device to the human body. An important aspect of the design is to avoid further injury development and permanent damage through long-term use [1]. Previous attempts to target this issue, tend to disregard aspects such as subject variability, simplification of complex human joints, and generalization of the human body's range of motion.

The challenges of alignment and fitting often dictate the exoskeleton design approaches. The joint-based design approach focuses on mimicking the human joints. Other designs focus on generating a specific task without having to align the exoskeleton to the corresponding human limb and joints. This is often referred to as the task-based design approach. In this study, both mechanisms are assessed and compared on their kinematic match and alignment to the human elbow joint with the use of musculoskeletal modeling and simulation software–OpenSim. The misalignment present in the designs, if any, will be quantified and used to evaluate and quantify the effects on the muscle-tendon length of the main flexor and extensor muscles while the elbow flexion-extension motion is simulated [2].

Exoskeleton Descriptions

Joint-Based Exoskeleton

The joint-based exoskeleton is a 5-Degree-of-Freedom (DOF) mechanism designed to assist with upper limb rehabilitation for patients who suffer from partial or full motor control impairments [15]. The mechanism (figure 1a) is composed of five links, where link 1, 4, and 5 are adjustable to account for anthropometric variability between users. The design also includes an adjustable stand to account for user height variability. The overall mechanism is composed of five joints that can generate different rehabilitation motion tasks such as shoulder flexion-extension, shoulder adduction-abduction, shoulder elevation-depression, and elbow flexion-extension. Moreover, a total of five motors drive the exoskeleton to generate the desired motion. Since the OpenSim software was utilized to perform the assessment, its Upper Extremity Dynamic Model was used to model the exoskeleton. Figure 1b demonstrates the exoskeleton with the human model.

FIGURE 1:

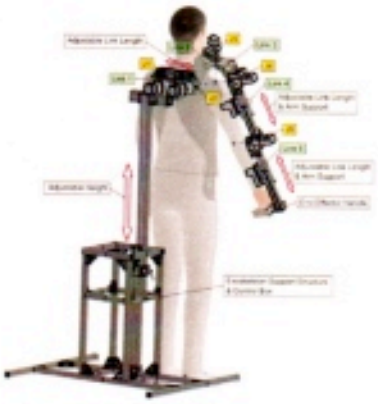

(a) Joint-based exoskeleton design

(b) OpenSim model, exoskeleton with human model

Task-Based Exoskeleton

The task-based exoskeleton is a 1-DOF parallel mechanism that was developed to generate the desired limb trajectory– elbow flexion-extension–for upper limb physical rehabilitation purposes [16]. The mechanism is composed of four links where one is fixed, and another is an end-effector. The fixed link is represented as the blue link and the end-effector is represented as the green link (Figure 2a). The mechanism is driven by a single motor located at the attachment point between links 1 and 3. All joints composing the task-based mechanism are modeled as revolute joints, which allow the driven elbow flexion-extension motion. Figure 2b demonstrates the exoskeleton with the Upper Extremity Dynamic Model in OpenSim.

FIGURE 2:

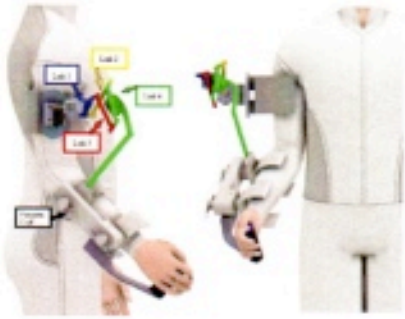

(a) Task-based exoskeleton design

(b) OpenSim model, exoskeleton with human model

An Assessment of the Elbow Joint

Once the exoskeletons were assembled and functional, the elbow flexion-extension motion was simulated from 44.079° to 125.634° using previously recorded motion capture data and the Inverse Kinematics toolbox in OpenSim. When the elbow flexion-extension simulation was acquired, the Body Kinematics toolbox by OpenSim was used to acquire information on the position of each part's origin throughout the generated motion. This enabled comparison of the position of the ulna's origin, located at the elbow joint, and its respective exoskeleton part—Link 5 and Link 3 for the joint-based and task-based exoskeletons, respectively. The maximum displacement values in the x, y, and z directions were then used to create a new human model where the position of the ulna was displaced with those values to observe the effects that the presented misalignment of each exoskeleton has on the tendon lengths of the main flexor and extensor muscles. The displaced human model is referred to as the misaligned human model, while the original human model is referred to as the healthy human model. Table 1 demonstrates the maximum position displacements for the joint-based and task-based exoskeletons.

Table 1: Maximum Position Displacement Values

Joint-Based Exoskeleton			**Task-Based Exoskeleton**		
x	y	z	x	y	z
-4.119mm	-14.227mm	4.883mm	11.4648mm	-4.5805mm	1.8640mm

The misaligned human model from each exoskeleton and the healthy human model were then simulated with the elbow flexion-extension motion and the Muscle Analysis toolbox by OpenSim was used to obtain information on the tendon lengths of the main flexor and extensor muscles throughout the motion. Out of the eight muscles observed, four muscles (brachialis, triceps medial, triceps lateral, and anconeus muscles) exceeded their elongation limit (Table 2). When the misalignments from the joint-based and task-based exoskeletons were simulated. On average, a muscle can elongate a maximum of 10% of its initial length prior to injury, hence, those values were found to further

assess the safety of the misalignments presented. The brachialis, triceps medial, triceps lateral, and anconeus had a maximum tendon length variation of 1.2717mm, 1.6091mm, 1.6091mm, and 1.2551mm, respectively. While the task-based exoskeleton demonstrated a maximum tendon length variation of 0.8717mm, 1.3272mm, 1.3272mm, and 1.1133mm for the same muscles, respectively.

Table 2: Muscle Elongation Limit to Avoid Serious Injuries to the Tendons

Muscle	Initial Tendon Length (mm)	10% (mm)
BRA	3.86	0.386
TRIlat	8.62	0.862
TRImed	7.38	0.738
ANC	6.98	0.698

Further assessments were completed to find a range of motion in which all muscle tendons performed safely. All muscles satisfied their tendon length limits when the elbow flexion-extension motion was generated from 44° to 70° and 44° to 100° for the joint-based and task-based exoskeleton, respectively. After the new range of motion was simulated, the brachialis, triceps medial, triceps lateral, and anconeus demonstrated a maximum tendon length variation of 0.295mm, 0.5478mm, 0.5478mm, and 0.4911mm, respectively for the joint-based exoskeleton, while the task-based exoskeleton demonstrated a maximum tendon length variation of 0.333mm, 0.8910mm, 0.8910mm, and 0.6925mm for the same muscles. Figure 3 demonstrates the variation in tendon length and pattern for the brachialis muscle of both exoskeletons, where the figure corresponding to the joint-based exoskeleton is labeled as "JB" and the one corresponding to the task-based exoskeleton is labeled as "TB".

FIGURE 3:

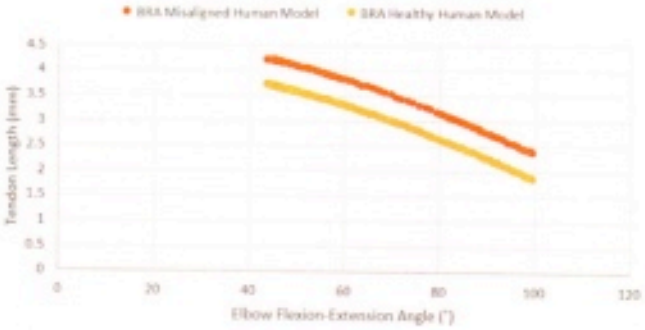

(a) JB brachialis

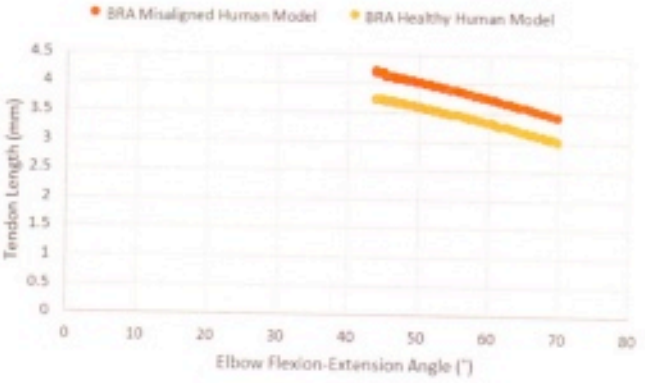

(b) TB brachialis

Conclusion

This study presented the assessment of joint-based and task-based exoskeletons for upper limb rehabilitation on their alignment to the human elbow joint using the OpenSim software. The observation throughout the assessment was focused on quantifying the misalignment present in the exoskeleton designs and the effects that the identified exoskeleton misalignments had on the muscle-tendon lengths within the main flexor and extensor muscles during the elbow flexion-

extension motion task. The results demonstrated that both exoskeletons had misalignments in the x, y, and z axes when compared to the human body. The task-based exoskeleton had less variation in tendon length overall when compared to the joint-based exoskeleton. However, both exoskeletons demonstrated a tendon length variation greater than the appropriate variation limit for the brachialis, triceps lateral, triceps medial, and anconeus muscles when the elbow flexion-extension motion was generated from 44° to 125°. It was later found that a smaller motion range of 44° to 70° and 44° to 100° would satisfy the elongation limit of all muscles observed for the joint-based and task-based exoskeletons, respectively. Nonetheless, based on the overall results, the task-based exoskeleton performed better than the joint-based exoskeleton during the assessment at the elbow joint.

References

Delgado, P., Alekhya, S., Majidirad, A., Hakansson, N. A., Desai, J., and Yihun, Y., 2020. "Shoulder kinematics assessment towards exoskeleton development". *Applied Sciences, 10*(18), p. 6336.

Delgado, P., Rincon, C., and Yihun, Y., 2022. "Human- exoskeleton joint coordination assessment: A case study on the shoulder and elbow joints". *Journal of Bionic Engineering (Accepted).*

Attampola Arachchige Don, T., 2021. "Development of an adaptive exoskeleton for upper arm rehabilitation." PhD thesis, Wichita State University.

Delgado, P., Arachchige Don, T. A., Gomez, J., Miranda, V., and Yihun, Y., 2021. "Design of bio-exoskeleton for elbow rehabilitation". In Frontiers in Biomedical Devices, Vol. 84812, American Society of Mechanical Engineers, p. V001T10A002.

Electrical Field Migration and Regulation of Glioma Cells

Audrey Scherrman *and*
Li Yao, PhD

Department of Biological Sciences, Wichita State University

Introduction

In the central nervous system (CNS), specialized stem cells called radial glia progenitors (RGPs) give rise to neurons that receive and transmit electrochemical signals, as well as glia that provides insulation and structural support to neurons (Merkle et al., 2004). Primary tumor cells in the CNS most commonly progenate from these two cell classes, glial cells especially, resulting in a wide range of histological subtypes as well as variances in patient prognosis and treatment plans (Rasband, 2016). While less prevalent, malignancies offer little over a 35% five-year survival rate due to their low chemotherapeutic responsiveness and difficulty in full surgical resection (Miller et al., 2021). The lack of treatment advancement warrants further investigation into the factors that may be responsible for CNS cancer invasion and metastasis.

Cell membranes mediate interactions and potentials between cells and their surrounding environments, and therefore play an important part in cell migration and cancer metastasis. This study aims to replicate factors that contribute to cell migration by exploring monolayer culture coating methods that mimic cell membrane microenvironments in a two-dimensional setting via adhesion-like sites on collagen and poly-D-lysine coated plates. Additionally, cell migration was observed and quantified in an applied electric field study as it has been reported that various cells exhibit endogenous electric fields as a result of changing ionic concentrations and membrane potentials, as seen in site-directed wound repair, and has now been linked to cancer growth (Nuccitelli, 2003, Xing et al., 2021). Studying the migratory behaviors of CNS tumors in these environments may help to elucidate some of the effectors of cancer metastasis within the central nervous system.

Methods

Migration of Tumor Cells in Electric Fields with Time-Lapse Imaging

To investigate the potential migration of neural cells in an endogenous electric field, U87 cells were cultured routinely in cell culture flasks and fed with Dulbecco's Modified Eagle Medium (DMEM) containing 1% penicillin/streptomycin, 10% horse serum, and 5% fetal bovine serum. Cell passages two through four were used for this experiment, and cells were cultured in a 37° C incubator with 5% CO_2. Once sufficiently passaged, cells were then cultured into non-coated culture dishes modified according to the following procedures.

Specialized culture chambers are necessary for electric stimuli to be applied. Therefore, to create these chambers, microscope slides were cut into fourths for a final size of 3 cm x 1 cm. Two of these cut slides were subsequently greased along one long edge and placed parallel to one another in the center of the dish, 1 cm apart to create a trough. A small plastic ladder is then placed inside the center, which creates a barrier for the cells to grow inside the trough and subsequently form adherence. The cells placed inside the chamber were then incubated at 37°C for 24 hours.

After cells were allowed to grow and adhere, the plastic ladder was removed, and a third coverslip was greased and added over the top to create a thin semi-enclosed channel only 0.5 mm deep. Additional grease was then applied thickly in lines perpendicular to the channel, covering the top and bottom, while leaving the channel mouth accessible, and extending to the edge of the dish to prevent further spread of cells and create a preliminary galvanic pool environment. Fresh medium was used to fill the top and bottom channel pools. The prepared culture dish was then placed inside a plastic incubator connected to a time-lapse microscope (Zeiss Axio Observer microscope) with 5% CO_2 at 37° C and with sterile conditions maintained throughout. NIH Image J software was used to analyze imaging in this experiment. With respect to the electric field, quantification of cell migration was used by a previously reported method (Yao et al., 2008).

To apply a stimulus from a direct current power source to the cultured cells, agar-salt bridges were created from Steinberg's solution and gelled with 1% agar. These bridges were used to connect silver-silver chloride electrodes in two beakers of Steinberg's solution to the galvanic chamber pools of the culture dish. Steady currents of 50mV were applied to the cells, images were taken by a digital camera (AxioCam MRm Rev.3 with FireWire) in five-minute intervals, and Zen2011 imaging microscope software was used to record the time-lapse image of the cell's migration. The migration was recorded for 1 hour with no current as a control, and then the stimulus was switched on and cells were recorded for an additional hour.

Well Plate Coating Conditions

To test favorable culture plate coatings as a migration study, PC12 cells were grown in two different conditions; cell culture plates coated with poly-D-lysine (100 ug/ml, Sigma-Aldrich, St. Louis, MO) and collagen-coated cell culture plates (20 mg/ml, Sigma-Aldrich, St. Louis, MO). All cells were then fed with a modified

concentration of DMEM and an additional 0.5% neural growth factor. Cell passages two through four were used for this experiment, and cells were cultured in the same conditions as the U87 line and recorded for two hours each using the software mentioned previously.

Results

Electric Stimulation Migratory Trends

The U87 cells used in this investigation showed tentative trends of migration. Figures 1A and 1B display migration tracks that have been superimposed over one another and coordinated with a four-quadrant X, Y axis. When time is equal to zero, it signifies the origin on the axis coordinate. Cells were tracked and quantified, each line representing a cell's displacement over a given timeframe. In a controlled environment with no stimulus, Figure 1A displays a migration grid indicating cells have a larger displacement along the ±Y axis. Figure 1B displays the migration patterns of cells in an environment with an electric stimulus applied and indicates a slight trend of the larger ±Y axis displacements skewing towards the ±X axis. Non-stimulated cells have a net migratory direction of -0.18, and stimulated cells have a net migratory direction of –0.02. Additionally, non-stimulated cells have a slightly higher net speed of 0.56 µm/min in comparison to stimulated cells with a net speed of 0.47µm/min.

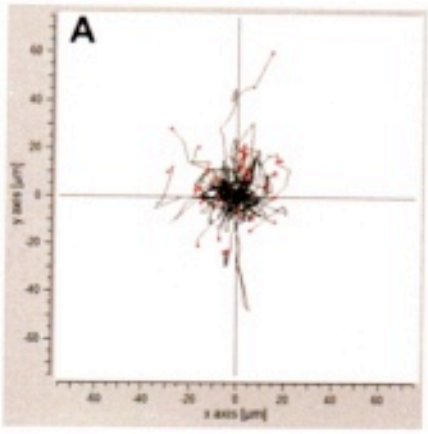

A) Control

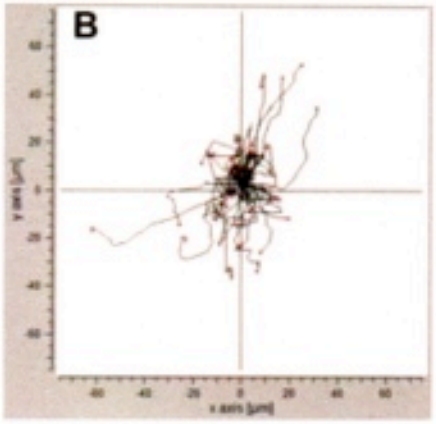

B) 1 hr of electric stimulus

Collagen Coated Plates Display Greater Migratory Behavior

PC12 cells display greater migratory behavior on collagen-coated well plates compared to poly-D-lysine coated plates. Cells were tracked for two hours per condition and were quantified and displayed using the superimposed image grid methods mentioned previously. The cells on the collagen-coated plate showed a net displacement of 42µm, while cells on the poly-D-lysine plate showed a net displacement of 13µm. Additionally, cells on the collagen-coated plate had a higher migration

speed of 0.25μm/min compared to 0.18μm/min for cells on a poly-D-lysine coated plate.

Figures 2A, 2B Poly-D-lysine vs collagen coating, Figures 2C, 2D not pictured, available on request.

Discussion

In this study, the migration patterns of CNS tumor cells were investigated by mimicking a cellular membrane associated environment via applied electric fields and culture plate coatings. While certain migratory trends can be observed in the electric stimulation study between the control group and the stimulus group, there is not enough evidence to suggest either cathode or anode directedness at this time. Further exploration of stimulus strength and duration variances as well as additional experimental replications would yield a more complete data set to examine for migratory behaviors. Supply chain of resources was a limitation for this project and prevented results from replication studies to be included here.

Regarding coated plate migratory behaviors, cells cultured on collagen coated plates display increased methods of motility in all tested areas when compared to poly-D-lysine coated plates. However, the poly-D-lysine coating method is still a suitable candidate for studying cell migratory behaviors as the cells display motility due to the increased attraction between electrostatic forces, similar to a cell membrane's ionic interactions. Furthermore, using this chemical as a coating method would not interfere with further downstream research applications such as protein extraction and subsequent RNA sequencing, which would be a potential drawback of the collagen protein method. These applications would then be a further research goal in terms of understanding the genes and signaling pathways that contribute to a cell's motility.

References

American Society of Clinical Oncology. (2022, January 6). *Central nervous system tumors (brain and spinal cord)* . Cancer.Net. Retrieved July 20, 2022, from https://www.cancer.net/cancer-types/central-nervous-system-tumors-brain-and-spinal-cord-childhood/introduction#:~:text=In%20most%20instances%2C%20CNS%20tumors,astrocytoma%2C%20oligodendroglioma%2C%20and%20ependymoma.

Merkle, F. T., Tramontin, A. D., García-Verdugo, J. M., & Alvarez-Buylla, A. (2004). Radial glia give rise to adult neural stem cells in the subventricular zone. *Proceedings of the National Academy of Sciences*, *101*(50), 17528–17532. https://doi.org/10.1073/pnas.0407893101

Miller, K. D., Ostrom, Q. T., Kruchko, C., Patil, N., Tihan, T., Cioffi, G., Fuchs, H. E., Waite, K. A., Jemal, A., Siegel, R. L., & Barnholtz-Sloan, J. S. (2021). Brain and other Central Nervous System Tumor Statistics, 2021. *CA: A Cancer Journal for Clinicians*, *71*(5), 381–406. https://doi.org/10.3322/caac.21693

Pilkington, G. J. (2005). Cancer stem cells in the mammalian central nervous system. *Cell Proliferation*, *38*(6), 423–433. https://doi.org/10.1111/j.1365-2184.2005.00358.x

Rasband, M. N. (2016). Glial contributions to neural function and disease. *Molecular & Cellular Proteomics*, *15*(2), 355–361. https://doi.org/10.1074/mcp.r115.053744

Li, X., Yang, F., & Rubinsky, B. (2021). A correlation between electric fields that target the cell membrane potential and dividing hela cancer cell growth inhibition. *IEEE Transactions on Biomedical Engineering*, *68*(6), 1951–1956. https://doi.org/10.1109/tbme.2020.3042650

Yao, L., Shanley, L., McCaig, C., & Zhao, M. (2008). Small applied electric fields guide migration of hippocampal neurons. *Journal of Cellular Physiology*, *216*(2), 527–535. https://doi.org/10.1002/jcp.21431